Spatial and temporal variability of the hydroxyl radical: Understanding the role of large-scale climate features and their influence on OH through its dynamical and photochemical drivers

Daniel C. Anderson[1,2], Bryan N. Duncan[2], Arlene M. Fiore[3], Colleen B. Baublitz[3], Melanie B. Follette-Cook[2,4], Julie M. Nicely[2,5], Glenn M. Wolfe[2]

[1] Universities Space Research Association, GESTAR, Columbia, MD, USA
[2] Atmospheric Chemistry and Dynamics Laboratory, NASA Goddard Space Flight Center, Greenbelt, MD
[3] Department of Earth and Environmental Sciences, Columbia University, Palisades, NY
[4] Morgan State University, GESTAR, Baltimore, MD
[5] Earth System Science Interdisciplinary Center, University of Maryland, College Park, College Park, MD

Correspondence to: Daniel C. Anderson (daniel.c.anderson@nasa.gov)

Abstract

The hydroxyl radical (OH) is the primary atmospheric oxidant, responsible for removing many important trace gases, including methane, from the atmosphere. Although robust relationships between OH drivers and modes of climate variability have been shown, the underlying mechanisms between OH and these climate modes, such as the El Niño Southern Oscillation (ENSO), have not been thoroughly investigated. Here, we use a chemical transport model to perform a 38-year simulation of atmospheric chemistry, in conjunction with satellite observations, to understand the relationship between tropospheric OH and ENSO, Northern Hemispheric modes of variability, the Indian Ocean Dipole, and monsoons. Empirical orthogonal function (EOF) and regression analyses show that ENSO is the dominant mode of global OH variability in the tropospheric column and upper troposphere, responsible for approximately 30% of the total variance in boreal winter. Reductions in OH due to El Niño are centered over the tropical Pacific and Australia and can be as high as 10 - 15% in the tropospheric column. The relationship between ENSO and OH is driven by changes in nitrogen oxides in the upper troposphere and changes in water vapor and O^1D in the lower troposphere. While the correlations between monsoons or other modes of variability and OH span smaller spatial scales than for ENSO, regional changes in OH can be significantly larger than those caused by ENSO. Similar relationships occur in multiple models that participated in the Chemistry Climate Model Initiative (CCMI), suggesting that the dependence of OH interannual variability on these well-known modes of climate variability is robust. Finally, the spatial pattern and r^2 values of correlation between ENSO and modeled OH drivers – such as carbon monoxide, water vapor, lightning, and to a lesser extent, NO_2 – closely agree with satellite observations. The ability of satellite products to capture the relationship between OH drivers and ENSO provides an avenue to an indirect OH observation strategy and new constraints on OH variability.

1.0   Introduction

The hydroxyl radical (OH), the atmosphere's primary oxidant, removes many trace gases that affect composition and climate. Despite its central role in atmospheric chemistry, the spatiotemporal distributions of OH concentrations are poorly constrained, often confounding interpretation of observed variations and trends of important atmospheric constituents. For example, there are several plausible explanations of the observed fluctuations in the global burden of atmospheric methane (CH_4), the second-most important anthropogenic greenhouse gas. Explanations include variations and trends in both emissions and oxidation of methane (Prather and Holmes, 2017;Rigby

60 et al., 2017;Turner et al., 2017). Better constraints on OH and its dynamical and photochemical
61 drivers are needed to improve confidence in our interpretation of recent methane trends and to
62 project future climate in response to changes in emissions and composition.
63
64 Observational limitations and chemistry climate model disagreement pose challenges to advancing
65 our understanding of the spatiotemporal variability in OH. There are few direct *in situ* OH
66 observations, on local, regional, and global scales (Stone et al., 2012) as OH is both highly reactive,
67 with a lifetime of ~1 s in the free troposphere (Mao et al., 2009), and low in concentration, on the
68 order of 10^6 molecules/cm^3. Recent work has demonstrated that formaldehyde, a longer-lived
69 species (hours) whose chemical production in the remote troposphere is dominated by CH_4
70 oxidation, shows promise for inferring variability in OH columns over the remote atmosphere
71 (Wolfe et al., 2019). In models of atmospheric chemistry and transport, OH can vary widely, with
72 differences in global methane lifetime, a proxy for OH abundance, between 45 and 80% among
73 models in inter-comparison projects (e.g., Voulgarakis et al., 2013;Nicely et al., 2017;Zhao et al.,
74 2019).
75
76 Analysis of the factors causing inter-model differences in the tropospheric OH burden is
77 challenging, as causation is difficult to prove with a species so tightly coupled to a multitude of
78 chemical and meteorological processes. Primary OH production occurs through photolysis of O_3
79 followed by reaction with water vapor ($H_2O_{(v)}$), while secondary production is often regulated by
80 nitrogen oxides (NO_X = NO + NO_2) through the reaction of the hydroperoxyl radical (HO_2) with NO.
81 Globally, CO and CH_4 are the primary sinks, although other species, particularly volatile organic
82 compounds (VOCs), can be important regionally. However, attributing OH variability remains
83 challenging, with different models showing widely ranging responses in OH to changes in these
84 drivers, particularly to NO_X and humidity (Wild et al., 2020).
85
86 These chemical and radiative drivers of OH variability are in turn partially regulated by large-scale
87 dynamical features, such as the El Niño Southern Oscillation (ENSO), monsoons, and modes of
88 Northern Hemispheric (NH) variability (*e.g.* the North Atlantic Oscillation (NAO)), through changes
89 in transport and emissions. Oman et al. (2011) and Oman et al. (2013) used satellite observations
90 and chemistry climate models to show that the horizontal and vertical distributions of tropospheric
91 ozone are significantly modulated by ENSO, most prominently through the manifestation of a dipole
92 pattern over southeast Asia and the tropical western Pacific. Sekiya and Sudo (2012) found similar
93 results with the CHASER chemical transport model, along with strong relationships between ozone
94 variability and the Indian Ocean Dipole (IOD), the Arctic Oscillation, and the Asian winter monsoon.
95 ENSO events can also change CH_4 emissions from wetlands (Zhang et al., 2018), lightning NO
96 production (Murray et al., 2013;Murray et al., 2014;Turner et al., 2018), and CO emissions from
97 biomass burning (Duncan, 2003a;Duncan, 2003b;Rowlinson et al., 2019). In addition to this
98 biomass burning relationship with ENSO, Buchholz et al. (2018) also noted relationships between
99 CO in tropical fire regions and the IOD as well as with the Tropical South Atlantic and Southern
100 Annular modes. Relationships between the Madden-Julian Oscillation (MJO) and variability of
101 tropical ozone (Tian et al., 2007;Ziemke et al., 2015), $H_2O_{(v)}$ (Myers and Waliser, 2003), and CO
102 (Wong and Dessler, 2007) have also been shown. Finally, climate modes can alter the long range
103 transport of CO to the Arctic, through increased outflow from Europe (Li et al., 2002;Creilson et al.,
104 2003;e.g. Duncan, 2004) and Asia (Fisher et al., 2010) for the NAO and ENSO, respectively.
105
106 Despite the strong linkages between these dynamical features and OH drivers, there is little
107 research on the relationship between these processes and OH itself. Turner et al. (2018) used a
108 6000-year simulation with free running dynamics to suggest that ENSO is the dominant mode of OH
109 variability at decadal timescales, mainly through its effects on lightning NO emissions. Their study,

116 however, held most forcings and emissions, including greenhouse gas concentrations and biomass
117 burning, to 1860 conditions. Emissions of lightning NO, dust, and dimethyl sulfide were allowed to
118 respond to model meteorology. During the 1997/98 ENSO event, increases in CO from biomass
119 burning led to decreases in OH of 9% on the global scale (Rowlinson et al., 2019) and up to 20%
120 over the Indian Ocean (Duncan, 2003a). Using inversions of observations of methyl chloroform to
121 estimate OH concentrations, Prinn et al. (2001) found OH to be lower during ENSO years,
122 suggesting this could be linked to reduced UV radiation near the surface due to increased cloud
123 coverage. As with ENSO, modeling studies have shown that the Asian monsoon increases OH
124 concentrations in the upper troposphere (UT) through increased lightning NO production, despite
125 increases in convectively lofted OH sinks, particularly CO (Lelieveld et al., 2018).
126
127 Here, we examine how OH and related chemical and radiative factors vary with known modes of
128 climate and atmospheric variability. Using correlation analysis, we compare the relationship
129 between ENSO and tropospheric column OH from the MERRA-2 GMI (Modern-Era Retrospective
130 analysis for Research and Applications Global Modeling Initiative) setup of the NASA Goddard Earth
131 Observing System (GEOS) Chemistry Climate Model (GEOSCCM) (Strode et al., 2019) and four
132 models that participated in the joint International Global Atmospheric Chemistry
133 (IGAC)/Stratosphere-troposphere Processes And their Role in Climate (SPARC) Chemistry Climate
134 Model Initiative (CCMI) (Morgenstern et al., 2017). After evaluating these relationships from the
135 MERRA2 GMI model with *in situ* and satellite observations, we explore further the relationship
136 between OH, its precursors, and ENSO. Finally, we expand the analysis to include not only ENSO
137 but also other modes of internal climate variability.
138
2.0   Methods
140 In this section, we outline the methodology used to understand the relationship between OH and
141 large-scale dynamical drivers. First, we describe the analysis methods used in Section 2.1. In
142 Sections 2.2 and 2.3, we describe the relevant details of the MERRA2 GMI and CCMI simulations,
143 respectively.
144
2.1   Description of Analysis Methods
146 Because the factors driving OH concentrations and interannual variability are altitude dependent,
147 we divide the atmosphere into 4 layers: the surface to the top of the PBL (PBL), from the top of the
148 PBL to 500 hPa (Lower Free Troposphere: LFT), between 500 and 300 hPa (Middle Free
149 Troposphere: MFT), and from 300 hPa to the tropopause (Upper Free Troposphere: UFT). Output
150 from each model has been vertically averaged to these layers on a seasonal basis. In addition, we
151 also examine the tropospheric column.
152
153 To help determine the relationship between the modes of climate variability and photochemical
154 and meteorological variables archived by the various models, we regress model output against
155 different climate indices. To perform the regression, we first detrend the output on a monthly
156 basis, removing any linear trend from each variable over the 1980 to 2018 period to account for
157 changes in the background value. We then regress the model variable against a specific climate
158 index (*e.g.* ENSO index) for 1980 to 2018. We perform these regressions on each grid cell for each
159 of the 4 layers as well as for the tropospheric column. In the results below, we only include
160 regressions where the Pearson correlation coefficient (r) exceeds 0.5, unless otherwise indicated.
161 Using other methods to define significance of a regression, such as a two-tailed student t test with p
162 values less than 0.05, does not significantly alter the results.
163

168 Climate features considered here include ENSO, the IOD, several Northern Hemispheric
169 atmospheric modes of variability, and various monsoons. We use monthly values of the ENSO
170 multivariate index (MEI) (Wolter and Timlin, 2011) obtained from https://psl.noaa.gov/enso/mei
171 and averaged to seasonal time scales. Here, ENSO-related events are defined according to the
172 seasonally averaged MEI, where MEI > 0.5 is an El Niño event, MEI < -0.5 is a La Niña event, and an
173 MEI value between 0.5 and -0.5 is a neutral event. For the Indian Ocean Dipole, we used the Dipole
174 Mode Index (DMI) obtained from https://psl.noaa.gov/gcos_wgsp/Timeseries/DMI/. Northern
175 Hemispheric modes considered are the NAO, the East Atlantic Pattern (EA), the Pacific North
176 American Pattern (PNA), the East Atlantic Western Russian Pattern, the Scandinavian Pattern, the
177 West Pacific Pattern, the East Pacific North Pacific Pattern, and the Tropical Northern Hemisphere
178 Pattern. Indices for the NH modes were taken from the NOAA Climate Prediction Center (available
179 online at https://www.cpc.ncep.noaa.gov/data/teledoc/telecontents.shtml) and were determined
180 from a rotated principal component analysis of the 500 hPa geopotential height of the National
181 Center for Environmental Prediction Reanalysis.
182
183 The MERRA2 GMI (Section 2.2) and CCMI models (Section 2.3) included here are constrained or
184 nudged to reanalyses data (MERRA, MERRA2, JRA-55, and the ERA-interim) which assimilate
185 observed meteorology. The meteorological variables used to calculate the DMI and MEI, including
186 sea surface temperature, sea level pressure, and zonal and meridional winds, agree well or are
187 identical among the different reanalyses (Orbe et al., 2020;Bosilovich et al., 2015). Thus, climate
188 modes in these models correspond to the NOAA indices. Likewise, indices for the NAO calculated
189 from surface pressure from the models correlate well (r^2 of 0.79 or greater) with the NAO index
190 calculated by NOAA.
191
192 **Table 1:** Summary of the climate modes and monsoons considered in this work. The index used to
193 characterize the mode, as well as the source of the index, is also indicated.

Mode Type	Index	Mode Type	Index
El Niño Southern Oscillation	Multivariate ENSO Index (NOAA)	North Atlantic Oscillation	EOF of geopotential height at 500 mbar from NCEP reanalysis (NOAA)
Indian Ocean Dipole	Dipole Mode Index (NOAA)	East Atlantic	
Asian Monsoon	Model-specific index calculated from the difference of zonal winds in monsoon specific regions	Pacific North American	
South American Monsoon		East Atlantic Western Russian	
North American Monsoon		Scandinavian	
South African Monsoon		West Pacific	
North African Monsoon		East Pacific North Pacific	
Australian Monsoon		Tropical Northern Hemisphere	
Western North Pacific Monsoon			

194
195 Monsoons included in this analysis are the Asian, South American, North American, South African,
196 North African, Australian, and the Western North Pacific. We calculate the monsoon index for each

Formatted: English (US)

Deleted: and

Deleted: for the Indian Ocean Dipole,

Deleted: https://psl.noaa.gov/enso/mei/ and

Deleted: , respectively

Deleted: Indian

model used in this study based on the definitions of Yim et al. (2013), where the index is defined by the difference of zonal winds at 850 hPa between two, monsoon-specific regions. See Table 2 in Yim et al. (2013) for more details. Because the MERRA2 GMI and CCMI models included here are constrained or nudged to different reanalyses, the calculated monsoon index varies among the models, although the indices of a given monsoon from each model are highly correlated with one another (generally r² > 0.9). Table 1 summarizes the climate modes and monsoons as well as the corresponding indices used here.

In addition to regression analysis, we also performed an empirical orthogonal function (EOF) analysis for tropospheric column OH (TCOH) and separately for each of the four layers described above. EOF analysis allows for the statistical determination of the spatial modes of OH variability and their variation with time without *a priori* knowledge of the controlling mechanisms (e.g., Barnston and Livezey, 1987). To perform the analysis, OH fields for each grid box were detrended by subtracting a linear fit to the time series over the 1980 to 2018 period to account for changes in background associated with long-term trends in OH. We report here only the first and second EOFs and their associated principal component time series as none of the other EOFs correlated spatially or temporally with any of the modes of climate variability discussed here.

2.2   MERRA-2 GMI Simulation Description

To understand the interannual variability of OH, we use the MERRA-2 GMI (Modern-Era Retrospective analysis for Research and Applications Global Modeling Initiative) simulation, publicly available at https://acd-ext.gsfc.nasa.gov/Projects/GEOSCCM/MERRA2GMI/. This is a run of the GEOSCCM model (Strode et al., 2019) constrained to meteorology from MERRA-2 (Gelaro et al., 2017) that uses the GMI chemical mechanism (Duncan et al., 2007;Oman et al., 2013;Gelaro et al., 2017). The GMI chemical mechanism includes approximately 120 species and 400 reactions, characterizing the photochemistry of the troposphere and stratosphere. The model was run from 1980 to 2018 at a resolution of c180 on the cubed sphere, equivalent to approximately 0.625° longitude × 0.5° latitude, with 72 vertical levels. The model was run in a replay mode (Orbe et al., 2017) and constrained to temperature, pressure, and winds from MERRA-2. Model output is available at daily and monthly resolutions, with hourly output available only for some local satellite overpass times. All data used in this work is monthly averaged unless otherwise indicated.

Anthropogenic emissions are from the Measuring Atmospheric Composition and Climate mega City (MACCity) inventory (Granier et al., 2011) for 1980 – 2010, and then from the Representative Concentration Pathway 8.5 (RCP8.5) scenario for 2011 – 2018. Biomass burning emissions are from the Global Fire Emissions Database (GFED) 4s inventory starting in 1997 (Giglio et al., 2013). Biomass burning emissions from before 1997 are calculated from scale factors derived from aerosol index data from the Total Ozone Mapping Spectrometer (TOMS) instrument, as described in Duncan (2003). Biogenic emissions are calculated online using the method described in Guenther et al. (1999) and Guenther et al. (2000), an early form of the Model of Emissions of Gases and Aerosols from Nature (MEGAN). A known high bias in isoprene emissions from MEGAN (e.g., Wang et al., 2017), could exacerbate low modeled OH in regions dominated by biogenic VOC emissions. Lightning NO emissions are based on the cumulative mass flux (Allen et al., 2010), with constraints from the Lightning Imaging Sounder (LIS)/Optical Transient Detector (OTD) v2.3 climatology (Cecil et al., 2014). Total, global lightning NO emissions are scaled to be 6.5 Tg N/year for each year of the simulation, although emissions demonstrate significant interannual variability on the local scale. For example, over the tropical Pacific, an area we will investigate throughout this paper, peak emissions are 1.5 times higher than minimum emissions over the time period studied here (Fig. S1). Methane concentrations are specified at the surface for 4 different latitude bands (90°S - 30°S, 30°S - 0°, 0° - 30°N, 30°N - 90°N) at monthly resolution and advected throughout the troposphere.

Deleted: GEOSCCM

Deleted: (Section 2.2)

Deleted: (Section 2.3)

Deleted: (MERRA, MERRA2, JRA-55, and the ERA-interim), …

Deleted: ¶

Deleted: and standardized with the standard deviation before calculating the EOF.

Deleted:

Deleted: Model of Emissions of Gases and Aerosols from Nature (MEGAN) model

Deleted: (Guenther et al., 1999;Guenther et al., 2000).

Deleted: as latitude- and time-dependent boundary conditions…

266 Methane data are from the NOAA Global Monitoring Division (GMD) surface network (Dlugokencky
267 et al., 1994) and monthly values are interpolated from annual means.
268
269 Because CH_4 is specified as a boundary condition, the model does not capture feedbacks (e.g.,
270 wetland or wildfire emissions) between CH_4 emissions and climate modes beyond the extent to
271 which these manifest in the observed methane surface concentrations. ENSO, for example, is
272 known to affect atmospheric CH_4 concentrations through changes in emissions from wetlands
273 (Zhang et al., 2018;Melton et al., 2013) and biomass burning (Worden et al., 2013), although there
274 is uncertainty in the magnitudes of these effects (Melton et al., 2013). On the global scale, however,
275 these ENSO-induced changes in emissions do not significantly perturb background CH_4. For
276 example, during the 1997/98 ENSO event, one of the largest on record, CH_4 grew at a rate of
277 approximately 15 ppbv/yr on top of a background on the order of 1700 ppbv (Nisbet et al., 2016).
278 Because of this small perturbation and the dominance of CO as the primary OH sink over much of
279 the globe (see Section 5.0), it is unlikely that the relationship between climate modes and OH would
280 differ significantly with the inclusion of direct methane emissions in the simulation.

281
282 **2.3   IGAC/SPARC Chemistry Climate Model Initiative (CCMI) Phase 1 Model Simulations**
283 To place the results from MERRA2 GMI in the context of other models, we compare our simulation
284 with those from CCMI. The CCMI was conducted to help assess the ability of a suite of models to
285 address various aspects of atmospheric chemistry, including trends in tropospheric ozone and the
286 controlling mechanisms of OH (Morgenstern et al., 2017). Output from these models have already
287 been used to assess various aspects of tropospheric OH (Zhao et al., 2019;Nicely et al., 2020), HCHO
288 (Anderson et al., 2017), O_3 (Revell et al., 2018;Dhomse et al., 2018) and meteorological variables
289 (Orbe et al., 2020). Modeling groups conducted multiple runs, including a forecast scenario to 2100
290 and two hindcast scenarios, one with free-running meteorology and one, the specified dynamics
291 (SD) scenario, in which models were either nudged to meteorological reanalyses or run as chemical
292 transport models (Orbe et al., 2020).
293
294 We perform a similar analysis as with MERRA2 GMI with four models that performed the CCMI SD
295 run. We use the SD run, which spanned the years 1980 – 2010, instead of the other scenarios to
296 allow for more direct comparison among the CCMI models as well as with MERRA2 GMI and
297 observations from satellite. We include only models that output data for all years between 1980
298 and 2010 and that have non-methane hydrocarbon chemistry in their chemical mechanisms.
299 Models used here are WACCM (Solomon et al., 2015), CHASER (MIROC-ESM) (Watanabe et al.,
300 2011), a setup of EMAC with 90 vertical levels (EMAC) (Jöckel et al., 2016), and MRI-ESM1r1
301 (Yukimoto et al., 2012). We omit CAM4Chem and a different setup of EMAC with 47 vertical levels
302 because results for those models are essentially identical to WACCM and EMAC90, respectively.
303 EMAC90 and CHASER were nudged to the ERA-interim reanalysis, WACCM to the MERRA
304 reanalysis, and MRI to the JRA-55 reanalysis. Sea surface temperatures (SST) and sea ice were
305 prescribed in each model with the Hadley SST dataset. Anthropogenic emissions were from the
306 MACCity inventory, while lightning NO_X was calculated online using model-specific
307 parameterizations. Biomass burning emissions are from Granier et al. (2011), which incorporate a
308 modified version of the RETRO inventory from 1980 – 1996 and GFEDv2 from 1997 – 2010 and are
309 based on Lamarque et al. (2010). Monthly-averaged CO emissions from this inventory in Indonesia,
310 where biomass burning emissions are strongly affected by ENSO (e.g., Duncan, 2003a), are highly
311 correlated (r^2 = 0.79) in time with the GFED 4s inventory used in the M2GMI simulation. Likewise,
312 monthly-averaged CO emissions over Indonesia from the two inventories agree within 35%, on
313 average. Further model details can be found in Orbe et al. (2020), Morgenstern et al. (2017), and

314 references therein.

317
318 As with the MERRA2 GMI analysis, we use monthly averaged output. For layer averaging, only
319 EMAC90, WACCM, and MRI output a tropopause height, while no models output PBL height. To
320 calculate the tropopause height for CHASER, we used the relationship between O_3 and CO as
321 described in Pan et al. (2004). PBL height for all models was determined from the bulk Richardson
322 number (Seibert et al., 2000).
323
324 **3.0 MERRA2 GMI Simulation Evaluation**
325 While there has been some evaluation of the MERRA2 GMI simulation (Ziemke et al., 2019;Strode et
326 al., 2019), species in the simulation relevant to this study have not been investigated. As a result,
327 we evaluate MERRA2 GMI using *in situ* observations of OH and related species as well as remotely
328 sensed observations of OH drivers in order to understand the effect any model biases could have on
329 our results. In Section 3.1, we use *in situ* observations from the first two deployments of the
330 Atmospheric Tomography (ATom) campaign to evaluate OH and CO over the remote Pacific and
331 Atlantic Oceans. In Section 3.2, we also compare output to satellite observations of CO, $H_2O_{(v)}$, and
332 NO_2 to evaluate the model over larger temporal and spatial scales.
333
334 **3.1   Evaluation of MERRA2 GMI with *in situ* Observations**
335 During the ATom campaign, a suite of air quality and climate relevant trace gases and aerosols were
336 measured throughout the remote Pacific and Atlantic. During each of the deployments, aircraft
337 transected the Pacific from Alaska to New Zealand, went around Tierra del Fuego, and travelled
338 north over the Atlantic to Greenland. Each flight consisted of a series of ascents and descents
339 allowing for vertical profiling across most latitudes of the remote Pacific and Atlantic Oceans. The
340 combination of the flight track and the repetition across seasons provided unprecedented sampling
341 of many trace gases, including OH. As part of the ATom campaign, a limited subset of species,
342 including OH and CO, from the MERRA2 GMI simulation were output hourly for the duration of
343 ATom1 (July – August 2016) and ATom2 (January – February 2017) only, allowing for direct
344 comparison to the *in situ* observations. Only daily or longer resolution output is available for the
345 other deployments, and, as a result, we focus our analysis on these first two deployments.
346
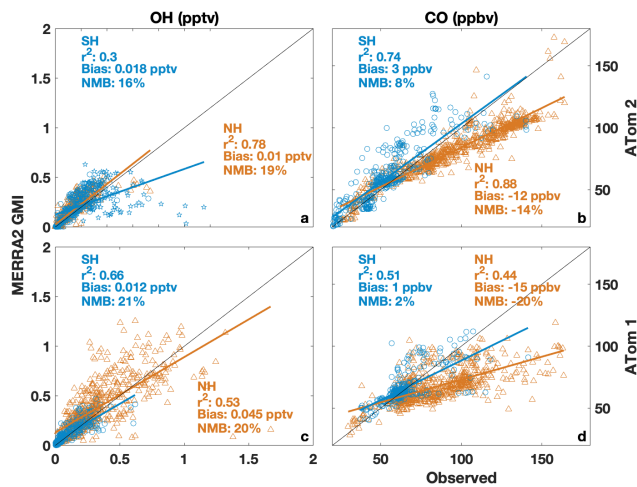
Figure 1: Regression of observed OH (left) and CO (right) from ATom 2 (boreal winter 2017; top row) and ATom 1 (boreal summer 2016; bottom row) against hourly output from MERRA2 GMI interpolated to the ATom flight track. Data from the Southern (blue circles) and Northern (orange triangles) Hemisphere are shown, along with the r², bias, and normalized mean bias (NMB) for each hemisphere. Observations and model output have been filtered for biomass burning influence. Observations of continental outflow from New Zealand and South America from ATom 2 are indicated by blue stars.

Observations used here include OH (Brune et al., 2020) and CO (Santoni et al., 2014), with 2σ uncertainties of 35% and 3.5 ppbv, respectively. Data have been averaged to a 5-minute time base and filtered for biomass burning influence, defined as times when concentrations of HCN and CO are both above the 75th percentile for the individual ATom deployments. We omit the biomass burning influenced parcels because small differences in measured and modeled winds could result in misplacement of modeled biomass burning plumes, resulting in unrealistically large differences in OH. Inclusion of the biomass burning influenced parcels does not significantly change the model bias but does degrade the correlation. For comparison of the observations to MERRA2 GMI, hourly data were output by the model and then bilinearly interpolated in the horizontal and linearly interpolated in time and in the vertical to the *in situ* observation time and location.

MERRA2 GMI has a OH high bias of approximately 20% (Fig. 1a) when compared to observations from ATom 2. A regression of measured and modeled OH shows moderate to high correlation in both the Southern Hemisphere (SH) and NH, with r² values of 0.30 and 0.78, respectively. Normalized Mean Biases (NMB) relative to the observations is within measurement uncertainty in both the NH (19%) and SH (16%), with nearly identical high biases during the summer deployment of ATom1 (Fig. 1c). The comparatively poorer model performance for OH in the SH is being driven by continental outflow from South America and New Zealand. When data from these regions are omitted (Fig. 1a, blue stars), the correlation for the SH increases to 0.63 and the NMB is 22%. The limited model output at hourly resolution does not allow for a determination of the cause of this disagreement in continental outflow regions. In the case of South America, however, a known high bias in modeled isoprene, resulting in extremely low OH over the Amazon, is consistent with the disagreement between the simulation and observations.

Agreement between observed and modeled CO shows a strong hemispheric dependence, with a NMB of -14% in the NH (i.e., the model is lower than observations by 14%) and 8% in the SH during ATom 2, although both hemispheres have a strong correlation ($r^2 > 0.7$). While agreement in the SH improves in ATom 1, with a NMB of 2% (Fig. 1d), the model underestimate in the NH is even more pronounced (NMB = -20%). This NH low bias in CO is a well-known problem in global chemistry models (e.g. Naik et al., 2013;Stein et al., 2014;Travis et al., 2020) and could be a contributing factor in the overestimate in OH, as CO is the dominant global OH sink.

Comparison of the MERRA2 GMI simulation to *in situ* observations demonstrates that the model captures the spatial variability of OH and its predominant global sink, CO, in the remote atmosphere during both the NH summer and winter, with the exception of OH off the coast of South America and New Zealand. The poorer agreement between measured and modeled OH in regions of fresh, continental outflow suggests that modeled relationships between climate modes and OH in these regions might be more uncertain than in the remote atmosphere. This lack of agreement does not significantly affect the results discussed in this work, as the majority of the relationships found between OH and modes of climate variability discussed in Sections 4 and 5 are centered in the remote atmosphere.

3.2   Evaluation of MERRA2 GMI with Satellite Observations

While there are no remotely sensed observations of tropospheric column OH (TCOH), there are satellite observations of OH drivers. Comparing these observations to MERRA2 GMI allows for model evaluation over larger spatial and temporal scales than with ATom. Satellite data used here include tropospheric CO columns from the Measurement Of Pollutants In The Troposphere (MOPITT) instrument, $H_2O_{(v)}$ from the Atmospheric Infrared Sounder (AIRS), and tropospheric NO_2 from the Ozone Monitoring Instrument (OMI). AIRS is on the Aqua satellite, with a daily, local overpass time of approximately 13:30. We use the monthly averaged, Level 3, Version 6 standard physical retrieval (Susskind et al., 2014) from 2003 to 2018. For MOPITT CO on the Terra satellite, we use the Level 3, V008 retrieval that uses both near and thermal infrared radiances (Deeter et al., 2019) from 2001 to 2018. MOPITT has a daily, local overpass time of approximately 10:30. Both satellite products have a global horizontal resolution of $1° × 1°$. We also use the OMI NO_2 Version 4, Level 3 product (Lamsal et al., 2021) from 2005 to 2018. Data have been regridded to $1° × 1°$ horizontal resolution. OMI is located on the Aura satellite and, as with AIRS, has a local overpass time of approximately 13:30.

For comparison of the satellite retrievals to MERRA2 GMI, we use monthly fields of the model variables output at the satellite overpass time. For CO, where averaging kernel and *a priori* information are available for the Level 3 MOPITT data, we convolve the model output with these variables so that direct comparison between satellite and model are possible. While shape factors and scattering weights for the OMI NO_2 retrieval are unavailable for the Level 3 data, shape factors for the OMI NO_2 retrieval are determined from a similar setup of the GEOSCCM model, also employing the GMI chemical mechanism and MERRA2 meteorology. Applying the satellite shape factors to the simulation discussed here would therefore not result in significant changes in the modeled NO_2. Finally, for AIRS $H_2O_{(v)}$, averaging kernel information was unavailable for the Level 3 data, so numerical comparisons between satellite and model should be regarded as more qualitative than quantitative.

When compared to MOPITT in boreal winter (*i.e.*, DJF), tropospheric column CO from MERRA2 GMI (Fig. 2, first column) shows similar results to that found through comparison to the *in situ* observations, namely a low bias in the NH (9%) and high bias in the SH (7%). Differences over the tropical Pacific, an area that will be shown later to have a strong relationship between ENSO and

445 OH, are generally less than 10%, while a noticeable high bias exists over parts of South America.
446 Results for June – August (JJA) are spatially similar (Fig. 3), with a NH low bias of 20% and
447 overestimates of column CO, averaging 45%, in the SH. These areas of high bias over South America
448 likely result from the high bias in isoprene emissions, as discussed in Section 2.2, that would lead to
449 unrealistically high *in situ* production of CO.
450
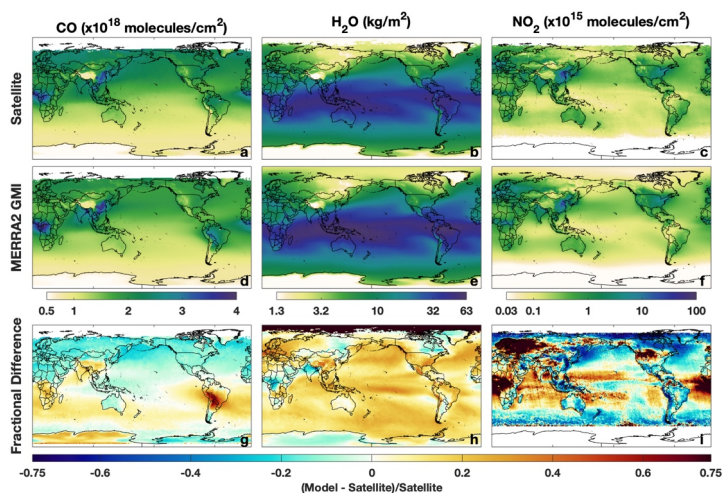
451
452 *Figure 2: Tropospheric column CO (left), H₂O$_{(v)}$ (middle), and NO₂ (right) from MOPITT, AIRS, and OMI, respectively (top row), and*
453 *MERRA2 GMI (middle row), for DJF. For the satellite retrievals and model, data are averaged over the time range described in the*
454 *text for each instrument. The fractional difference between MERRA2 GMI and the satellite is shown in the bottom row.*

455 MERRA2 GMI captures the spatial distribution of H₂O$_{(v)}$, although the model is biased high in both
456 the column and throughout much of the troposphere. Overestimates in column H₂O$_{(v)}$ are ~14% in
457 both December – February (DJF) (Fig. 2h) and JJA (Fig. 3). These overestimates extend over most of
458 the world's oceans, and only small regions over northern India, central Africa, eastern Russia, and
459 eastern Canada show any underestimate in H₂O$_{(v)}$. Fractional differences in H₂O$_{(v)}$ between
460 MERRA2 GMI and the different AIRS pressure levels are most pronounced in the tropical UT (Fig.
461 4). At pressures greater than 700 hPa, modeled H₂O$_{(v)}$ is generally within 10% of the observations,
462 while for pressures less than 500 hPa, modeled H₂O$_{(v)}$ in the equatorial region disagrees with
463 observations by 55% on average.
464
465 Agreement between observed and modeled NO₂ is weaker than for the other species examined
466 here. While MERRA2 GMI appears to capture the regions with local NO₂ maxima – notably those
467 over central Africa, eastern China, and the northeastern United States – the magnitudes frequently
468 differ. The simulation shows a significant high bias over central Africa and the equatorial Atlantic
469 on the order of 100%, suggesting that biomass burning emissions of NO$_X$, the dominant NO source
470 in this region, are too high. In contrast, concentrations over eastern Asia are too low in the model,
471 suggesting errors in the anthropogenic emissions inventory and/or in the NO$_X$ lifetime. Strode et al.
472 (2019) also evaluated NO₂ in MERRA2 GMI, comparing trends in tropospheric column NO₂ over the
473 eastern US and eastern China in MERRA2 GMI and OMI. They found that although trends were
474 similar between the simulation and observations in both regions, the magnitude of the trends
475 differed, likely due to errors in the MACCity emissions inventory.
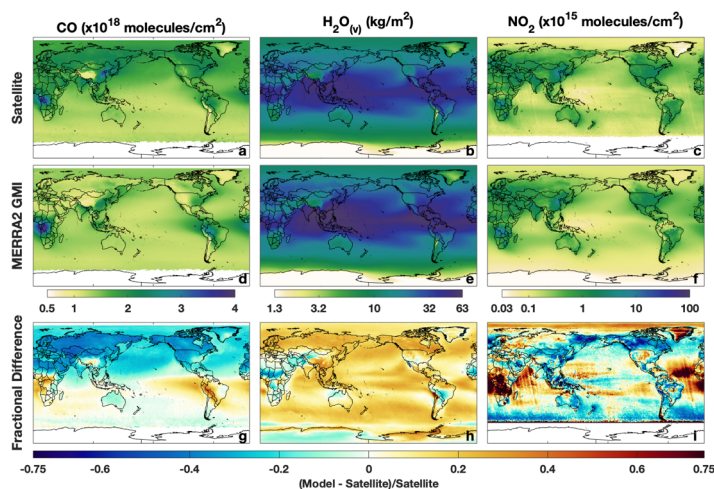
Figure 3: Same as Figure 2 except for JJA.

As with the *in situ* observations, comparison between MERRA2 GMI and satellite retrievals demonstrates that the simulation is able to capture the distribution of the chemical drivers of OH in remote regions, which tend to exhibit the strongest relationship between OH and climate modes (see Section 4.0). These results lend confidence to the analysis described in Sections 4.0 and 5.0 and suggest the findings in remote regions are likely applicable to the actual atmosphere. The large disagreement between the simulation and observed column CO and NO_2 in regions that are significantly impacted by biomass burning and/or biogenic emissions suggests, however, that modeled relationships of chemical species with modes of climate variability in these regions should be viewed with caution. We further evaluate the ability of the simulation to capture the relationship between ENSO and CO, $H_2O_{(v)}$, and NO_2 using satellite observations in Section 5.1.2.
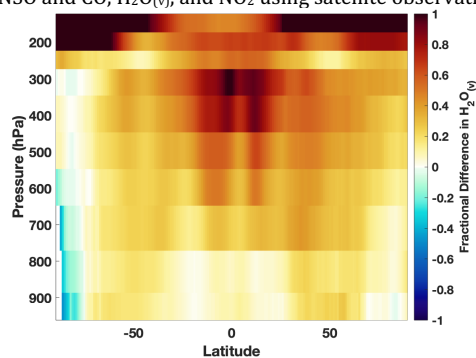
Figure 4: The fractional difference in zonal mean $H_2O_{(v)}$ between MERRA2 GMI and AIRS for the different AIRS pressure layers for DJF. Positive numbers indicate a high bias in the model.

4.0   The Relationship between Simulated OH Variability and Climate Modes

When considered in concert, the modes of climate variability evaluated here (i.e., ENSO, the IOD, and NH modes) along with monsoons explain a substantial fraction of the simulated tropospheric OH interannual variability over 19 – 40% of the global troposphere by mass, depending on season. Figure 5 highlights regions that show significant correlation between TCOH and the NH modes (purple), monsoons (light blue), ENSO (green), and the IOD (orange) for each season in MERRA2 GMI output. In all seasons, correlation with ENSO has the largest spatial extent, but in DJF and MAM, for example, the 8 NH modes can explain TCOH variability over large swaths of the NH, comprising 10% of global, tropospheric mass. In JJA, the combination of the different climate modes and monsoons has the smallest spatial coverage (19% of the global, tropospheric mass), while the IOD, consistent with its seasonal variability, only has a widespread correlation with TCOH during SON. Similar patterns are found for the individual layers (Fig. S2).

Below, we examine the relationships between tropospheric OH and the various modes of climate variability demonstrated in Figure 5. First, in Section 5.0, we show that El Niño events lead to global reductions in tropospheric OH, with changes being driven by decreased secondary production in the UFT that more than compensates for increased primary production in the PBL. In Section 6.0, we demonstrate that the effects on OH from NH modes of variability, the IOD, and some monsoons have limited spatial scales, as compared to ENSO, but can significantly alter local OH distributions. In both sections, we also compare simulations from MERRA2 GMI to simulations from the CCMI, demonstrating that the relationship between OH and climate modes is robust among multiple models.
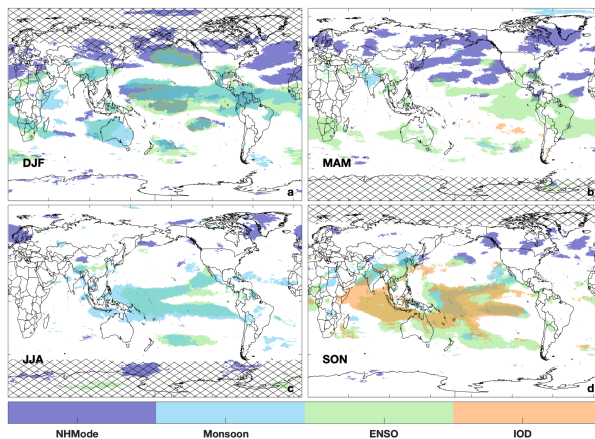
Figure 5. Regions that show a significant correlation (absolute value of r >0.5) between a NH mode (purple), monsoon (light blue), ENSO (green), or IOD (orange) and TCOH for each season in the MERRA2 GMI simulation. Regions with TCOH less than 1 x 10^{11} molecules/cm² have been hatched out.

5.0 Relationship between Simulated OH Variability and ENSO in MERRA2 GMI

To understand the relationship between OH, its drivers, and ENSO, we first investigate the OH production rate. In the MERRA2 GMI simulation, the OH production rate is primarily dependent on reactions 1 – 4, where O^1D is produced from the photolysis of tropospheric O_3. In the free troposphere, these four reactions comprise at least 95% of OH production in the tropics, on average, and at least 90% in the PBL. Only in the regions with large biogenic emissions (e.g., South America and central Africa) do other reactions contribute more than 15% of the total OH

Deleted: atmosphere
Formatted: Font: (Default) Cambria, 11 pt
Deleted: Figure 4

Deleted: the globe
Deleted: climate modes
Deleted: have
Deleted: e
Deleted: 4
Formatted: Font: (Default) Cambria, 11 pt
Deleted: Figure 4
Deleted: increased primary production in the PBL and

Deleted: 4
Deleted: n

548 production in the PBL. As will be shown, the effects of ENSO on OH are primarily focused away
549 from these regions, so we restrict our analysis to reactions 1-4.
550

$$H_2O_2 + h\upsilon \rightarrow 2OH \qquad\qquad\qquad \text{(Reaction 1)}$$
$$NO + HO_2 \rightarrow NO_2 + OH \qquad\qquad\qquad \text{(Reaction 2)}$$
$$O_3 + HO_2 \rightarrow 2O_2 + OH \qquad\qquad\qquad \text{(Reaction 3)}$$
$$H_2O + O^1D \rightarrow 2OH \qquad\qquad\qquad \text{(Reaction 4)}$$
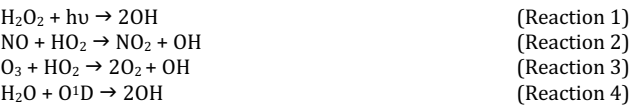
551
552 During El Niño events, the dominance of these individual reactions in producing OH varies with
553 altitude. We focus our analysis on DJF throughout Section 5.0 because that is the season with the
554 largest impact of ENSO on OH as shown in Figure 5. Figure 6 shows the zonal mean of the fraction
555 of total OH production from the $H_2O + O^1D$ (a) and $NO + HO_2$ (b) reactions as well as the total OH
556 production rate (c) during El Niño events in DJF. While the production rates along these pathways
557 vary with the ENSO phase, as discussed in Sections 5.2 and 5.3, the relative importance of the
558 individual reactions is similar during neutral and La Niña events (not shown) and is in agreement
559 with previous model studies (e.g. Spivakovsky et al., 2000).
560
561 The $H_2O + O^1D$ reaction is dominant from the surface to about 800 hPa through much of the SH and
562 the tropics, while, near the surface, the $NO + HO_2$ reaction only has large impacts in the NH mid-
563 latitudes. This influence of NO_X in the NH mid-latitudes extends through much of the troposphere.
564 In the UFT, this reaction is the greatest contributor to total OH production at all latitudes except the
565 NH polar region, where the $HO_2 + O_3$ reaction dominates during polar night (Fig. S3). Total OH
566 production in the polar regions, however, is orders of magnitude lower than in the tropics. Outside
567 of the polar regions, the $HO_2 + O_3$ and H_2O_2 photolysis reactions generally contribute between 10
568 and 30% of the total rate (Fig. S3). The dominant OH sink throughout the troposphere is CO, which
569 is responsible for 50% or greater of OH loss at all tropospheric pressures and latitudes (Fig. S4)
570 during El Niño events. Because of the differing importance of the individual OH production
571 reactions with altitude, we first examine the relationship between OH and ENSO for TCOH (Section
572 5.1) and then separately for the PBL (Section 5.2) and the UFT (Section 5.3). Finally, in Section 5.4,
573 we investigate the MFT and LFT, where the effects of ENSO on OH are more limited.
574
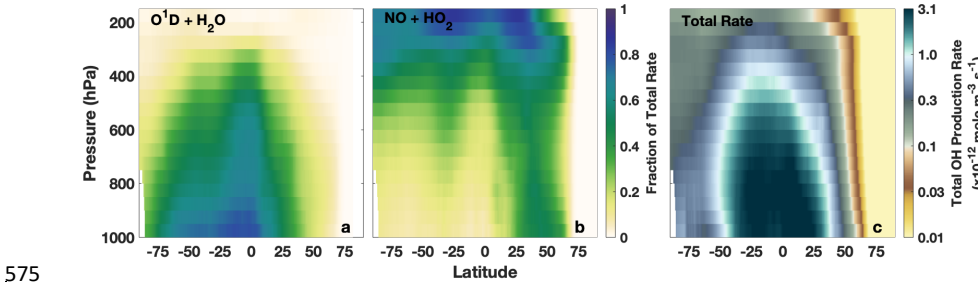
575
576 *Figure 6. Zonal mean of the fractional contribution of the $O^1D + H_2O$ (a) and $NO + HO_2$ (b) reactions to the total OH production*
577 *rate as well as the total OH production rate (c) for El Niño events (MEI > 0.5) for DJF averaged over 1980-2018.*

578 **5.1   Tropospheric Column OH**
579 **5.1.1   The Relationship between Simulated TCOH and ENSO**

Moved (insertion) [2]
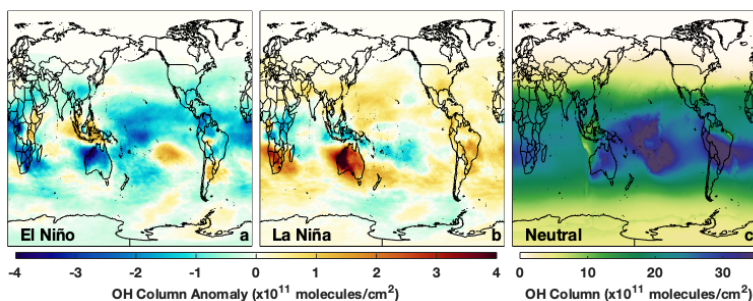
594
595 *Figure 7: Absolute difference in TCOH between El Niño events and neutral events (a) for DJF averaged over 1980 – 2018. El*
596 *Niño and neutral events are defined as a season having an MEI value greater than 0.5 or an MEI value between -0.5 and*
597 *0.5, respectively. The analogous plot for La Niña events (MEI less than -0.5) is also shown (b). Panel c shows the average OH*
598 *column for neutral events.   The 1980 – 2018 time period includes 11 El Niños, 12 La Niñas, and 15 neutral events in DJF.*

599 As shown in Figure 7, TCOH decreases by 3.3% during El Niño events (relative to neutral events)
600 equatorward of 30° in DJF and is characterized by widespread decreases in the tropics and
601 subtropics, especially northern Australia, and west-central and southern Africa. Regional increases
602 are found over eastern Africa, the east-central Pacific, southern South America, and Indonesia.
603 Maximum decreases in TCOH are on the order of 4.5×10^{11} molecules/cm^2 ($\sim$10-15%) and are
604 centered over northern Australia, while maximum increases in TCOH ($\sim 2.5 \times 10^{11}$ molecules/cm^2)
605 are centered over Sumatra.
606
607 During La Niña events, TCOH increases relative to neutral events over much of the globe, although
608 the changes are not necessarily symmetric with those seen during El Niño events. Increases over
609 Australia are on the order of 1 to 2×10^{11} molecules/cm^2, on par with the decreases seen during El
610 Niño, but the changes during La Niña are centered over Western Australia and the Indian Ocean.
611 Over the Pacific, the magnitude of the OH increase is lower (on the order of 0.5 to 1×10^{11}
612 molecules/cm^2) than the decreases found during El Niño, and some regions off the coast of Hawaii
613 and Papua New Guinea show decreases during both ENSO phases. Besides these two regions, there
614 are also significant decreases in OH over eastern Africa and in the southern portion of South
615 America.
616
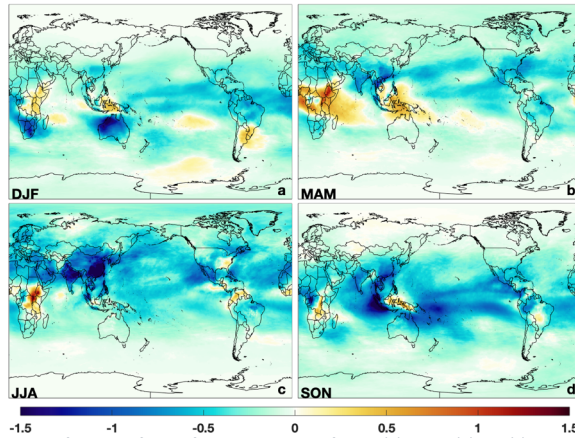
Figure 8: The first EOF of TCOH from MERRA2 GMI for DJF (a), MAM (b), JJA (c), and SON (d).

Consistent with these widespread changes in TCOH, EOF analysis demonstrates that over most seasons, JJA being the notable exception, ENSO is the dominant mode of OH variability. Figure 8 shows the spatial component of the first EOF of TCOH for the four seasons. While EOF analysis does not quantify changes in column content, it does highlight, for each mode of variability, regions where changes in TCOH are most prominent. For DJF, the first EOF (Fig. 8a) is almost identical to the composite figure showing OH anomalies during El Niño (Fig. 7a). Likewise, the temporal component of the 1st EOF strongly correlates with the MEI ($r^2 = 0.70$, Table 2). In DJF, the first EOF is responsible for 29% of the total spatial variance for TCOH. Although ENSO is the dominant mode, however, 70% of the spatial variance is still unexplained. In JJA, ENSO influence on OH is much weaker, with a correlation between the 1st EOF and TCOH of $r^2 = 0.25$, consistent with the seasonal cycle of ENSO.

While the spatial pattern of the EOF varies seasonally (Fig. 8), ENSO shows similar levels of correlation to the temporal component of the 1st EOF in MAM and SON as for DJF, with r^2 values of 0.54 and 0.60, respectively. Likewise, the spatial patterns of the first EOF of TCOH for these seasons are similar to the composite figures showing OH anomalies during El Niño (Fig. S5). For MAM, again the EOF shows regions with a negative sign over much of the Northern Hemisphere, with the largest magnitude centered over the Pacific Ocean, India, and Atlantic coast of the United States. Regions with an opposite sign include the Maritime Continent and much of central Africa. In SON, almost all of the tropics show some response, with major centers off the east coast of Papua New Guinea and off the west coast of Sumatra. In addition, there is a larger response over the Indian Ocean than for other months, also evident in the regression of TCOH with the MEI, suggesting the possible influence of the IOD, which is correlated with ENSO ($r^2 = 0.30$). This seasonal component in the strength of the relationship between the EOF and the MEI is also reflected in the correlation analysis (Fig. 5), where the area of correlation between TCOH and the MEI maximizes in DJF and minimizes in JJA.

Table 2: For each season, we show the r^2 of the correlation of the temporal component of the EOF that has the highest correlation with the MEI for TCOH and for OH in each layer. In addition, we also indicate the percent of the total spatial

667 *variance explained by that EOF. With the exception of the values indicated by a *, the 1st EOF has the highest correlation with*
668 *the MEI. Those indicated with a * are the 2nd EOF.*

Month	Column Pct. Variance	Column r^2	UFT Pct. Variance	UFT r^2	MFT Pct. Variance	MFT r^2	LFT Pct. Variance	LFT r^2	PBL Pct. Variance	PBL r^2
DJF	29.4	0.7	37.6	0.73	20.8	0.81	11.7*	0.55	12*	0.85
MAM	25.9	0.54	36.2	0.61	23.4	0.40	9.5*	0.48	9.3*	0.59
JJA	30.7	0.25	44.6	0.14	29	0.15	27.7	0.06	39.4	0.07
SON	33.2	0.60	41.1	0.50	22.8	0.63	12.3*	0.59	9.3*	0.63

669

670 **5.1.2 The Relationship between TCOH Drivers and ENSO**
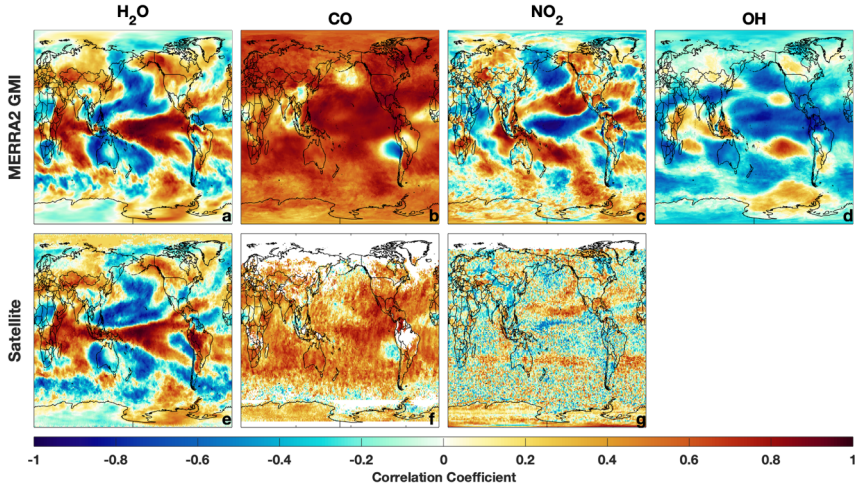
671
672 *Figure 9: Regression of tropospheric column $H_2O_{(v)}$ (a), CO (b), NO_2 (c), and OH (d) from MERRA2 GMI (top) and satellite retrievals*
673 *from AIRS (e), MOPITT (f), and OMI (g) against the MEI for DJF over the satellite lifetime.*

674 To understand the factors driving ENSO-related changes in TCOH, we also investigate the
675 relationship between OH precursors and ENSO. Figure 6 demonstrates that the $O^1D + H_2O$ and $NO +$
676 HO_2 reactions control zonal mean OH production in the tropics. As a result, we investigate the
677 relationship between tropospheric column $H_2O_{(v)}$, CO, NO_2 and ENSO using both MERRA2 GMI
678 output and satellite retrievals. We use NO_2 here, instead of NO, because of its observability from
679 space, although simulated NO demonstrates similar spatial correlation patterns with the MEI as
680 simulated NO_2.

681

682 Regression of total column $H_2O_{(v)}$ from AIRS against the MEI (Fig. 9e) reveals a tri-pole pattern over
683 the Pacific Ocean, with an area of positive correlation throughout much of the equatorial Pacific
684 Ocean and areas of anti-correlation poleward of this region, in agreement with previous work (e.g.
685 Shi et al., 2018). Each of these areas is well-captured by the MERRA2 GMI simulation (Fig. 9a),
686 showing nearly identical spatial patterns and strength of correlation over most of the globe. This
687 relationship between $H_2O_{(v)}$ and ENSO can be explained by the increased convective uplifting in the
688 equatorial Pacific and associated increased subsidence poleward of this region during El Niño
689 events. While the anticorrelation between $H_2O_{(v)}$ and the MEI over Australia and southern Africa is

consistent with the decrease in TCOH over these regions during El Niño events (Fig. 7), the positive correlation between $H_2O_{(v)}$ and the MEI over the equatorial Pacific suggests there must be competing effects from other OH drivers in order to explain the decreases in TCOH in this region.

Simulated tropospheric column NO_2 is strongly anti-correlated with ENSO over the equatorial Pacific, indicating a suppression of OH production when the MEI is positive (El Niño), consistent with Figure 7. Column NO_2 exhibits the opposite correlation pattern as $H_2O_{(v)}$ over the Pacific, with decreases in NO_2 in regions with increased $H_2O_{(v)}$ and vice versa. The similarities in the spatial correlation patterns for NO_2 and $H_2O_{(v)}$ with the MEI suggests that convection is also at least partially driving the changes in NO_2 in the equatorial Pacific. Changes in the Walker Circulation associated with El Niño events have been shown to redistribute O_3 in the tropics, resulting in a dipole pattern over the western and central Pacific (Oman et al., 2011). Analysis of vertical winds and the NO_2 anomaly suggests a similar mechanism for NO_2.

Correlations between OMI NO_2 and the MEI suggest similar relationships as found in the MERRA2 GMI simulation, although the correlations are not as robust as for the other satellite variables examined here. This is likely because tropospheric NO_2 columns over the ocean are frequently at or below the instrumental average noise (5×10^{14} molecules/cm²). As with the simulation, OMI suggests broad regions of anti-correlation between ENSO and NO_2 in the equatorial Pacific and Gulf of Alaska as well as a region of positive correlation in the extra-tropical NH Pacific. These results demonstrate that, with enough temporal and spatial averaging, OMI is capable of capturing the variability of tropospheric NO_2 even in remote regions with low concentrations.

Tropospheric column CO and the MEI are positively correlated over most of the globe in both MERRA2 GMI and in MOPITT (Figs. 9b and f, respectively), suggesting strong increases in CO during El Niño events. This increase in CO is associated with increased biomass burning, particularly in Indonesia, and is consistent with the modeled decrease in OH (e.g. Duncan, 2003a) and with the widespread decrease in TCOH over much of the tropics.
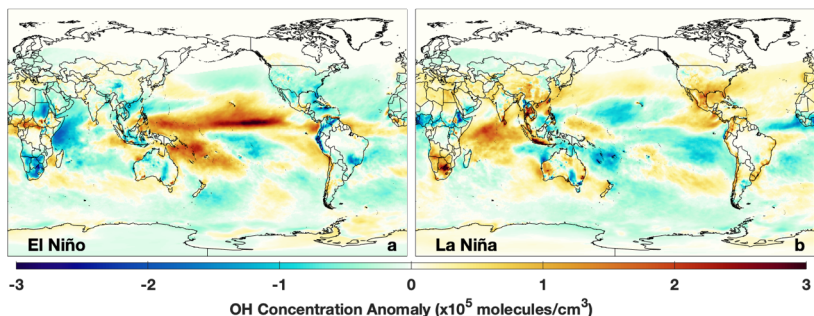
Figure 10: Same as panels a and b of Figure 7 except for the PBL level.

5.2   The Planetary Boundary Layer
5.2.1 The Relationship between PBL OH and ENSO

In contrast to the tropospheric column (Fig. 7), mean mass-weighted OH (e.g., Lawrence et al., 2001) in the PBL increases globally by 1% during El Niño events (Fig. 10), although regional differences are significantly larger. PBL OH exhibits an area of strong positive correlation with the MEI (Fig. 11d) over the central Pacific, marked by increases in concentrations on the order of 2-3 × 10⁵ molecules/cm³, approximately 15% higher than concentrations in neutral events. Changes in

Deleted: 6

Deleted: Figure 6

Formatted: Font: Cambria, 11 pt

Deleted: (Fig. S6)

Deleted: OMI data are insufficient to evaluate the simulated relationship between ENSO and column NO_2 based on our criteria of filtering data below the monthly averaged noise in the NO_2 retrieval

Deleted: .

Moved up [2]: The dominant OH sink throughout the troposphere is CO, which is responsible for 50% or greater of OH loss at all tropospheric pressures and latitudes (Fig. S7) during El Niño events.

Deleted: 8

Deleted: 9

Deleted: Figure 6

Deleted: 6

Deleted: 3

Deleted: equatorward of 30°

Deleted: 9

Deleted: the geographic extent of these changes is more limited than for TCOH

Deleted: 10

Deleted: years

760 the PBL during La Niña are smaller, with localized concentration decreases of about 5 – 10% over
761 the tropical Pacific (Fig. 10b). Regions with significant correlation between PBL OH and the MEI are
762 distinctly smaller than in the UFT (Fig. 11) and for TCOH (Fig. 5a), further emphasizing the
763 comparatively limited spatial effects of ENSO in the PBL.
764
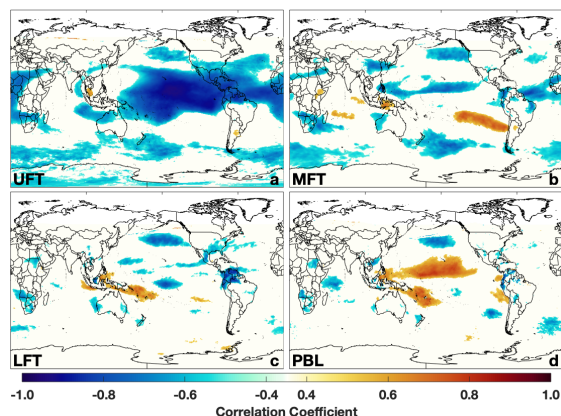
765
766
Figure 11: Correlation of OH from MERRA2 GMI with the MEI for the different atmospheric layers in DJF.

767 The more geographically limited changes in OH shown by the composite and regression analyses
768 are consistent with EOF analysis. During all seasons except JJA, ENSO correlates more strongly with
769 the 2nd EOF for the PBL (Table 2), suggesting another mechanism is the dominant mode of
770 variability. The spatial pattern of the 2nd EOF for PBL OH varies markedly across seasons (Fig. S6),
771 with the largest signal over the tropical Pacific during DJF and MAM and over Indonesia in SON. In
772 general, the r^2 with ENSO is 0.5 or higher and the mode contributes approximately 10% of the total
773 spatial variance, although correlation in JJA (r^2 = .07) is negligible.
774
775 In contrast to the ENSO-related EOFs, the first EOF (Fig. S7) for the DJF PBL layer reveals a spatial
776 pattern much more limited to continental regions and areas of continental outflow, suggesting that
777 this mode of variability is potentially reflective of long-term emission trends, in both anthropogenic
778 and biomass burning emissions. This is more evident in the 1st EOF for JJA, where the spatial
779 pattern shows opposite signs over regions with known net emissions reductions (the United States,
780 portions of Europe, and Japan) and those with known net emissions increases (China, India, the
781 Middle East) over the 1980 – 2018 period examined here.
782
783 **5.2.2 The Relationship between PBL OH drivers and ENSO**
784 Approximately 80% of the zonal mean OH production in the tropical PBL during El Niño events is
785 from the H_2O + O^1D reaction (Fig. 6a). Figure 12 shows the correlation of the MEI against both OH
786 production from this reaction as well as the total OH production rate for the PBL. Similar plots for
787 the other OH production reactions are shown in Figure S8. The nearly identical regression pattern
788 for the H_2O + O^1D and the total production rate with the MEI demonstrates that changes in this
789 reaction are driving changes in OH in the tropics during El Niño events.
790
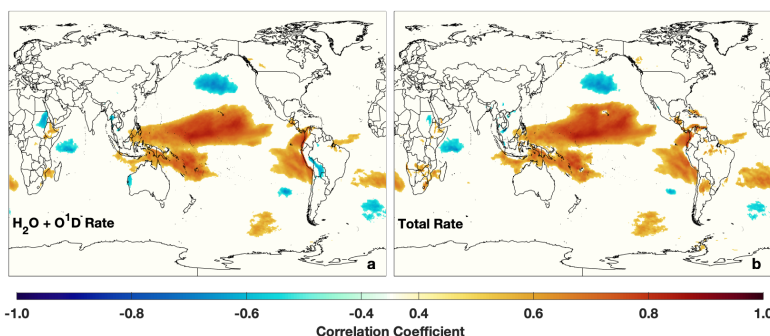
Figure 12: Correlation of the MEI with the production rate of OH from the H_2O + O^1D reaction (a) for DJF and the total OH production rate as defined in the text (b) for the PBL level are shown.

To understand the relationship between the OH production rate and ENSO in the PBL, we examine the changes in $H_2O_{(v)}$ and O^1D (Fig. 13). The spatial correlation of $H_2O_{(v)}$ and the MEI in the PBL exhibits a tripole pattern similar to that seen in the tropospheric column (Fig. 9a). While $H_2O_{(v)}$ is correlated with the MEI in the equatorial Pacific, which would lead to increases in OH production, $H_2O_{(v)}$ is anti-correlated with the MEI near the Hawaiian Islands and in the south Pacific, which would lead to decreased OH production in these regions. Because OH increases in these areas during El Niño events, the decreased $H_2O_{(v)}$ is offset by increases in O^1D to result in a net positive correlation of the total OH production rate.
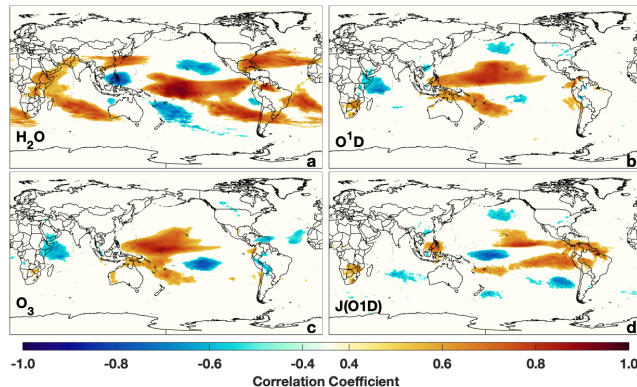
Figure 13: Correlation of the indicated species with the MEI for the PBL level for DJF.

Changes in O^1D and its photochemical drivers, O_3 and the rate of O_3 photolysis to O^1D ($J(O^1D)$), are driving the ENSO-related changes in OH in the PBL. O^1D shows distinct regions of positive correlation with ENSO extending from the Philippines to the eastern Pacific Ocean and another region of positive correlation off the coast of Papua New Guinea (Fig. 13b). O^1D abundance is controlled both by O_3 concentrations and incoming solar radiation at wavelengths less than 320 nm. Positive correlation between ENSO and O_3 in the PBL is limited to the western Pacific Ocean, where horizontal advection of relatively high O_3 air from Indonesia to the Pacific Ocean is increased during El Niño events due to changes in the Walker Circulation (Oman et al., 2011). Changes in O_3

838 and O^{1}D off the coast of Papua New Guinea are potentially linked to the South Pacific Convergence
839 Zone, which has a strong dependence on ENSO (Borlace et al., 2014). J(O^{1}D) exhibits two regions of
840 positive correlation extending from South America, one that reaches Hawaii in the NH and another
841 that spans almost to the coast of Australia in the SH (Fig. 13d). The MERRA2 GMI simulation shows
842 reduction in total stratospheric column O$_3$ of 2-5% in the tropics during El Niño, consistent with
843 previous work (e.g., Randel et al., 2009) which could contribute to the increase in J(O^{1}D), although
844 more work is needed to establish this link.
845

846 **5.3   The Upper Free Troposphere**
847 **5.3.1   The Relationship between UFT OH and ENSO**

Figure 14: Same as Figure 7 except for the UFT.

848
849
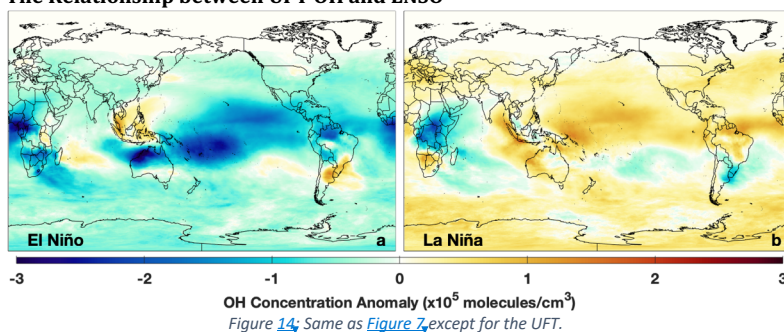
850 Similar to the relationship between ENSO and TCOH, OH in the UFT shows a strong anticorrelation
851 with the MEI over much of the tropics (Fig. 11a) resulting in large-scale decreases during El Niño
852 events. Decreases are highest over Northern Australia and the west-central Pacific, on the order of
853 1-2 × 10^5 molecules/cm^3 or 15-20% lower than in neutral events. During La Niña events, OH
854 increases with respect to neutral events over much of the globe, although the magnitude of the
855 increases is lower than for El Niño events. As with TCOH, one notable exception is over central
856 Africa, where UFT OH decreases between 1-2 × 10^5 molecules/cm^3.
857

858 EOF analysis on UFT OH followed by correlation of the temporal component (*i.e.,* the principal
859 component) with the MEI demonstrates that ENSO is the dominant mode of OH variability in the
860 UFT throughout much of the year. The MEI correlates with UFT OH (r^2 > 0.5) for DJF, MAM, and
861 SON, and explains 36% of the spatial variance or greater in each of the seasons (Table 1),
862 demonstrating that the relationship between ENSO and OH is even stronger in the UFT than in the
863 tropospheric column as a whole. As with the other atmospheric levels, there is little correlation
864 between OH and the MEI for JJA.
865

866 **5.3.2 The Relationship between UFT OH drivers and ENSO**
867 While changes in the O^{1}D + H$_2$O reaction drive ENSO-related changes in OH production in the PBL,
868 the NO + HO$_2$ reaction drives OH production in the UFT. The nearly identical correlation patterns
869 between the NO + HO$_2$ reaction (Fig. 15) and the total OH production rate in the UFT layer suggest
870 that changes in NO and/or HO$_2$ during El Niño are driving interannual OH variability in the UFT,
871 leading to decreased OH production over most of the tropical Pacific. This dependence on the NO +
872 HO$_2$ reaction is consistent with its overall contribution to the total production rate as shown in
873 Figure 6. Similar plots for the other OH production reactions are shown in Figure S9. While J(O^{1}D)
874 does increase in the UFT during El Niño events, as does production from the O^{1}D + H$_2$O reaction in

Deleted: 12

Formatted: English (US)

Deleted: These increases in O^{1}D are likely associated with changes in stratospheric O$_3$, which can decrease by several Dobson Units in the tropics during El Niño events

Deleted: .

Deleted: *13*

Deleted: *Figure 6*

Deleted: 10

Deleted: years

Deleted: years

Deleted: 14

Formatted: Font: Cambria, 11 pt

Deleted: Figure 5

Deleted: 10

some regions, the relatively small contribution of this reaction to the total OH production in the UFT (Fig. 6a) does not significantly perturb OH in this layer.

Regression analysis suggests that changes in NO are driving the relationship between OH and ENSO in the UFT in MERRA2 GMI. The MEI-NO correlation exhibits a strong dipole pattern in the tropics (Fig. 16), with areas of positive correlation over southeast Asia and the maritime continent and a large area of anti-correlation over much of the Pacific. HO_2 exhibits the opposite pattern, with increased concentrations over much of the Pacific during El Niño. This is consistent with the NO pattern, as decreased NO concentrations favor partitioning of HO_X ($HO_X = OH + HO_2$) towards HO_2.
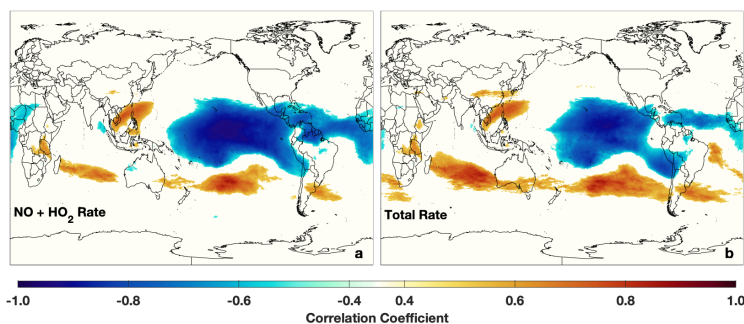
Figure 15: Correlation of the production rate of OH from the NO + HO_2 reaction (a) for DJF and the total OH production rate as defined in the text (b) with the MEI for the UFT level are shown.

Similarities between NO and O_3 correlation with the MEI in the UFT suggest similar mechanisms in controlling the spatial distribution of these species. The relationship between O_3 and the MEI shown in Figure 16b is similar to that found in Oman et al. (2013) using satellite data. They demonstrated that areas of increased O_3 over Indonesia coincided with increased downward flow in the region associated with changes in the Walker circulation. Decreases in O_3 over the Pacific coincided with increased upward motion, convectively lofting low O_3 air throughout the column. Similarly, regions of anomalously low NO in the UFT during El Niño events are associated with regions of anomalous upward motion, suggesting that decreases in upper tropospheric NO results from the convective lofting of NO_X-poor air from lower in the tropospheric column.
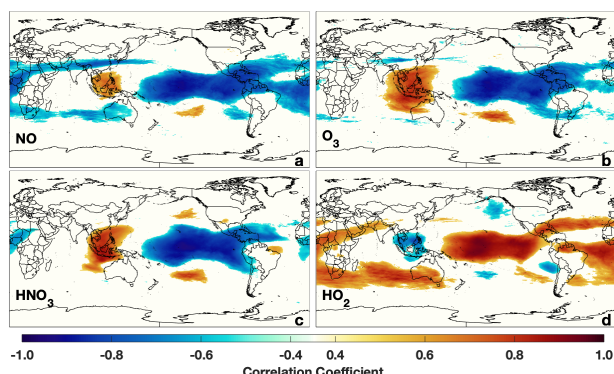
Figure 16: Correlation of the indicated species with the MEI for the UFT level for DJF.

Deleted: 15

The anti-correlation between ENSO and NO also suggests that lightning emissions of NO over the tropical Pacific do not significantly increase OH production in the region during El Niño events. Lightning NO emissions in MERRA2 GMI show a correlation pattern (Fig. 17) similar to that of $H_2O_{(v)}$ (Fig. 9a), with increased lightning over the equatorial Pacific and decreased lightning poleward of this region during El Niño events. The correlation pattern from MERRA2 GMI output agrees closely with flash rate data observed from the Lightning Imaging Sensor (LIS). The only region of significant difference between the satellite and MERRA2 GMI is in the equatorial Pacific, where the region of positive correlation extends from Papua New Guinea to the South American coast in the simulation but only about half that distance in the satellite product.

Deleted: does

Formatted: English (US)

Deleted: Figure 17

Deleted: 8

Deleted: c

Moved down [1]: These results are in contrast to the findings of Turner et al. (2018), who found that lightning NO emissions were the primary driver in the relationship between OH and ENSO. This difference could result from differences in the handling of biomass burning emissions in the two models, as MERRA2 GMI emissions were based on observations and varied seasonally. Our analysis also cannot disentangle the impact on ENSO-related changes in lighting NO emissions over land on OH in the remote atmosphere. ¶

Figure 17: The regression of lightning NO emissions at 300 hPa (a) and the lightning flash rate from the LIS/OTD time series (b) against the MEI. Lightning data are restricted to within 35 degrees of the equator because of the spatial coverage of the Tropical Rainfall Monitoring Mission (TRMM) satellite, on which LIS is located.

Deleted: 16

This tri-pole correlation pattern between MEI and lightning, evident in both the satellite and model (Fig. 17) is in contrast to the relationship with NO (Fig. 16a) and other reactive nitrogen (NO_y) species in the UFT. While the anti-correlation in NO is consistent with the changes in lightning NO emissions in some regions, in the equatorial Pacific band, NO decreases during El Niño events despite an increase in lightning NO emissions. This apparent discrepancy occurs because even though lightning NO increases by 100% or more over the equatorial Pacific during El Niño events in the model, the absolute difference is orders of magnitude lower than the accompanying changes over land. We conclude that the resulting NO perturbations over the equatorial Pacific latitudes are dominated by mechanism other than the local lightning response, such as changes in the Walker Circulation and the associated transport of air originating over the continents. This mechanism is supported by the similar regression pattern of longer-lived species, such as HNO_3 (Fig. 16c) and PAN (not shown), to NO in the UFT, showing that transport of reactive nitrogen from other source regions, particularly lightning over South America, is likely reduced during El Niño events.

Our findings are broadly consistent with Turner et al. (2018), who found that increases in lightning NO emissions drive increases in OH during La Niña and, conversely, decreases in lightning NO emissions lead to OH decreases during El Niño. The results presented here suggest that in addition to this influence of lightning locally, other mechanisms, such as atmospheric transport of NO_y species, also likely contribute to the relationship between ENSO and OH in the equatorial Pacific.

5.4   Variability in the MFT and LFT

As in the UFT, ENSO is the dominant mode of variability in the MFT in DJF, with strong correlation between the MEI and the temporal component of the first EOF ($r^2 = 0.81$) and the first EOF explaining 20.8% of the total spatial variance. Likewise, the largest OH anomalies in the LFT during both El Niño and La Niña are centered over Australia and South Africa (Fig. 18), similar to patterns seen in the UFT. Unlike in the UFT, however, there is a large region extending from the coast of South America into the Pacific where OH concentration is positively correlated with ENSO. These changes are driven by increase in $H_2O_{(v)}$, and subsequent increased OH production from the H_2O + O^1D reaction.
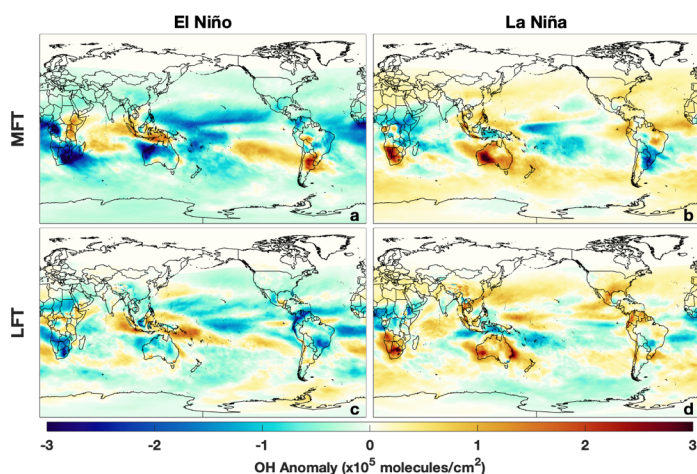
Figure 18: Same as panels a and b of Figure 7 except for the MFT and LFT.

1015 ENSO-related changes in OH concentration in the LFT are smaller in magnitude than for the other
1016 atmospheric levels (Fig. 18), with maximum increases in OH during El Niño on the order of 1 – 1.5 x

1017 10^5 molecules/cm^3. The spatial extent of significant correlation between the MEI and OH
1018 concentration in the LFT is smaller than for the other atmospheric levels (Fig. 11), with the most

1019 prominent feature being an area of positive correlation near Indonesia. Consistent with the more
1020 limited impact, ENSO is correlated with the 2nd EOF of OH concentration for the LFT (r^2 = 0.55),
1021 explaining only 11.7% of the total variability (Table 1).
1022
1023 It is likely that competing effects from the different drivers limit the interannual variability in OH in
1024 the LFT and MFT, explaining the smaller regions of correlation with ENSO. For these levels, no
1025 single OH production reaction clearly explains the relationship between ENSO and OH. In contrast
1026 to the PBL and UFT, where the relationship between the total OH production rate closely mirrored
1027 the production rates from the $O^1D + H_2O$ and $NO + HO_2$ reactions, respectively, there are no
1028 analogous relationships for the LFT and MFT. At these levels, no reaction clearly dominates total
1029 OH production (Fig. 6). Increases in H_2O in the mid troposphere, which would tend to increase OH,

1030 are offset by decreases in NO and O_3. These competing effects likely explain why the absolute
1031 changes in OH are comparatively smaller in the LFT than in the other layers.
1032
1033 The comparatively smaller changes in LFT OH during El Niño events limit the effect of ENSO on the

1034 interannual variability of the CH_4 lifetime. Global mean, mass-weighted tropospheric OH decreases
1035 by 2.2% during El Niño events, corresponding to only a 1% decrease in the CH_4 lifetime. While
1036 changes in OH concentration are most pronounced in the UFT and PBL, CH_4 lifetime is mostly
1037 dictated by OH in the LFT due to the temperature dependence of the $OH + CH_4$ reaction rate. This
1038 limited effect on CH_4 lifetime highlights the importance of investigating the spatial OH variability as
1039 global mean metrics can obscure important year-to-year changes.
1040
1041 **5.5   Comparing Simulated OH Relationships with ENSO in MERRA2 GMI with the CCMI**
1042 **models**
1043 To understand whether the relationship between OH and ENSO found in MERRA2 GMI is robust, we
1044 examine model simulations from the CCMI. To compare the relationship between OH and ENSO
1045 among the different models, we performed the same regression analysis on TCOH for the 4 CCMI
1046 models considered here as for MERRA2 GMI. Figure 19 shows the number of CCMI models that

1047 demonstrate a meaningful correlation between TCOH and the MEI, defined as the absolute value of
1048 r greater than 0.5, for each grid cell. To facilitate comparison, OH for each model has been
1049 regridded to the resolution of the model with the lowest horizontal resolution (2.81° longitude x
1050 2.77° latitude). This regridding does not substantially alter the correlation patterns examined here.
1051
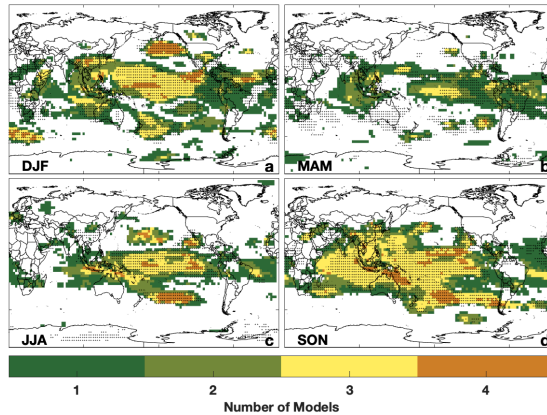
Figure 19: The number of CCMI models that show a correlation between TCOH and ENSO over the period 1980 to 2010. Only regressions with an absolute value of r greater than 0.5 are included. All models have been regridded to a common horizontal grid. This regridding does not substantially alter the correlation patterns examined here. Grid boxes that also exhibit significant correlations between TCOH and ENSO for MERRA2 GMI are indicated by the stippling.

In agreement with MERRA2 GMI, TCOH varies with ENSO over a large fraction of the tropics in most of the CCMI models, with broadly similar spatial regression patterns for most models across all seasons except for MAM (Fig. 19). In DJF, most models show strong correlation between ENSO and column OH over the central Pacific and south of the Aleutian Islands, with at least three CCMI models and MERRA2 GMI showing correlation in each of these areas. This agreement highlights the relationship of OH with ENSO as well as with the PNA and Australian monsoon, as discussed in Section 6.0. Similar agreement among models was found for SON and JJA, although the spatial extent of the highly correlated region is much smaller for JJA. In SON, the expansion of the area of significant correlation over most of the Indian Ocean likely results from the strong relationship between the IOD and ENSO during this season. There is less agreement in MAM, with only 1 or 2 models showing strong correlation in most regions.

EOF analysis of the different CCMI models likewise suggests that, in DJF, ENSO is the dominant mode of TCOH variability. The spatial pattern of the first EOF of TCOH in DJF for the five models is shown in Figure S10, and the principal component time series, along with the time series of the MEI, is shown in Figure S11. MERRA2 GMI, WACCM, and MRI show a strong correlation between the MEI and the first EOF ($r^2 > 0.64$). For each of these models ENSO is the cause of 29 – 48% of the total spatial variance in TCOH. The correlation between the first EOF and the MEI for CHASER is weaker ($r^2 = 0.28$), although the spatial component shows similarities to the other models. Correlation between the MEI and the EOFs for the UFT and MFT levels increases to 0.56 and 0.45, respectively, showing that ENSO is still important in controlling the interannual variability of CHASER, at least in the UFT. Similarly, EMAC has no correlation between the 1st EOF of TCOH and the MEI, but does for the UFT layer ($r^2 = 0.64$). This EOF explains 20% of the total spatial variance for this level but has a substantially different spatial pattern than for the other models. While further work is needed to understand the cause of the relationship between OH and ENSO in the UFT in EMAC, results from MERRA2 GMI suggest a role for changes in production via the NO + HO$_2$ reaction.

The agreement among the majority of the models suggests that the relationship between ENSO and TCOH is robust. While SSTs and emissions are identical among the models, meteorology, chemical mechanisms, and parameterizations, such as that for lightning and convection, vary widely. Despite the differences in these chemical and dynamical drivers of OH, the spatial patterns of the ENSO TCOH relationship are similar for most models. While it is beyond the scope of this paper, determining the cause of inter-model differences in this relationship between OH and climate modes could further our understanding of the mechanisms driving interannual OH variability. Given the results from the MERRA2 GMI analysis, investigating ENSO-related changes in UFT NO, both from lightning and transport, could provide insight into these inter-model differences. Further, Nicely et al. (2020) showed that $J(O^1D)$ was the largest driver in differences in the methane lifetime in the CCMI models, suggesting the potential importance of this variable in inter-model differences in the OH-ENSO relationship in the PBL and lower troposphere.

6.0 Relationship between simulated OH and NH Climate Modes, Monsoons, and the IOD

We now investigate the relationship between OH and the NH modes of variability, monsoons, and the IOD. In Section 6.1, we evaluate the relationships in MERRA2 GMI, demonstrating that these other climate features exert a much more spatially limited influence on OH as compared to ENSO (Fig. 5). Despite the comparatively limited extent of influence, each of these modes of variability can strongly influence the atmospheric oxidative capacity on the local scale. In Section 6.2, we compare the results from MERRA2 GMI to CCMI simulations, demonstrating that the relationship between OH and the IOD and NH modes is robust among models, while the relationship between monsoons and OH is primarily limited to MERRA2 GMI.

6.1 Simulated OH and the NH Climate Modes, Monsoons, and the IOD in MERRA2 GMI

Northern Hemispheric modes of variability are strongly correlated (r>0.5) with OH over ~10% of the globe during DJF but have a comparatively smaller effect on global OH than ENSO. During the positive phases of the NAO, defined as the index being greater than 0.4, TCOH increases by up to 25% in the northern Atlantic. Similarly, during the positive phase of the PNA, TCOH decreases by 10 – 20% in the northern Pacific (Fig. 20). Because OH production is almost an order of magnitude lower in the NH mid-latitudes than in the tropics (Fig. 6c), however, the resultant decrease in global mean mass-weighted OH (e.g., Lawrence et al., 2001) during the positive phase of the NAO is only 0.77%, as compared to decreases of 2.2% during an El Niño event. Similar results are found for the other NH modes.
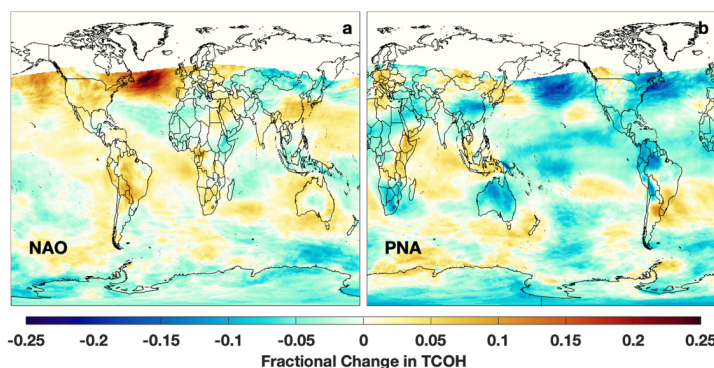
Figure 20: Fractional change in TCOH for positive phases of the NAO (a) and PNA (b), defined as having an index greater than 0.4, as compared to neutral events (index between -0.4 and 0.4). Note that, for emphasis, the x-axis is shifted in panel b to center the map over the Pacific Ocean.

The effects of the monsoons on OH interannual variability are much more localized than for ENSO and vary markedly among the different monsoons (Fig. S12). For example, Figure S13a shows the partial correlation coefficient (e.g., Sekiya and Sudo, 2012) of TCOH with the Australian monsoon, taking into account the correlation of the Australian monsoon index with the MEI, which has an r^2 of 0.65 for DJF. Correlation is almost exclusively restricted to areas near the Australian continent. In this region, however, monsoons with an index in the 75th percentile or higher result in TCOH that is 15-20% (up to 7×10^{11} molecules/cm^2) higher than for monsoons with an index between the 25th and 75th percentile (Fig. S14). These increases in OH column for the strongest monsoons are larger in magnitude than typical changes associated with ENSO, although they are limited to a smaller region, suggesting that the Australian monsoon can significantly perturb the local atmospheric oxidative capacity.

In contrast, despite its larger scale, the Asian monsoon only shows correlation with TCOH over a small portion of the subcontinent (Fig. S12b&d). Correlations outside of the sub-continent region result from the correlation between the Asian monsoon and ENSO. Interestingly, this correlation is only present during MAM and SON, not during JJA when the Asian monsoon is at full strength. Lelieveld et al. (2018) have shown using *in situ* observations that upper tropospheric OH is increased during the Asian monsoon. The lack of correlation demonstrated here suggests that the model is not accurately capturing the chemical variability within the monsoon anticyclone. The correlation with the monsoon index for MAM and SON could result from interannual variability in the start and end of the monsoon. Since these seasons are at the fringe of the monsoon, yearly variations in the start and end date would lead to larger variability than that seen during JJA, when the monsoon is active every year.

The IOD also shows a strong relationship with OH, although due to its annual cycle, the relationship is only present during SON (Fig. 5d). Taking into account the correlation between ENSO and the IOD ($r^2 = 0.30$), the partial correlation between the Dipole Mode Index (DMI) and TCOH becomes mostly restricted to the western Indian Ocean (Fig. S13b), where TCOH is anticorrelated with the DMI, resulting in decreases in TCOH on the order of 10% (about 1.5×10^{11} molecules/cm^2). During the positive phase of the IOD, the Indian Ocean basin exhibits a Walker-type circulation with anomalous surface easterly winds and increased convection in the region that exhibits

anticorrelation between OH and the DMI. This region is also characterized by an anticorrelation between the DMI and OH production from the NO + HO$_2$ reaction despite a positive correlation with lightning NO emissions, analogous to the relationship between NO and ENSO in the equatorial Pacific. This suggests that the anticorrelation between TCOH and the DMI in the eastern Indian Ocean is being driven by changes in NO transport from this Walker-type circulation. More work is needed, however, to prove this relationship, as the correlations between OH production from the NO + HO$_2$ reaction and the DMI do not meet our stated statistical significance criteria.

6.2 Simulated OH and the NH Climate Modes, Monsoons, and the IOD in the CCMI models

The MERRA2 GMI and the CCMI simulations exhibit nearly identical spatial relationships between TCOH and the NH climate modes and the IOD, demonstrating that these relationships are robust among multiple models. For example, all 5 models show two broad regions of correlation between the NAO and TCOH, corresponding to the dipole pattern of the NAO (Fig. 21a). Similar agreement is found for the other NH modes (Fig. S15). Likewise, most models show the same pattern of correlation between the IOD and TCOH (Fig. 21b), consistent with their agreement for ENSO since the two modes are closely related.
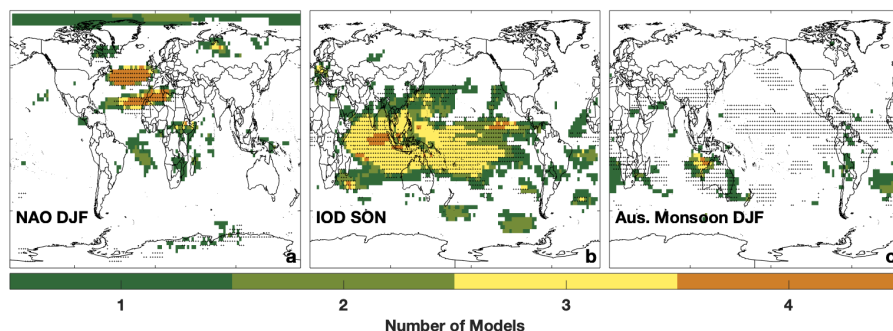
Figure 21: Same as Figure 19 except for the NAO (a) the IOD (b), and the Australian Monsoon (c). The NAO and Australian monsoon are shown for DJF and the IOD for SON..

In contrast to the other modes of variability, the relationship between TCOH and the different monsoons varies widely among the models. Agreement is highest for the Australian monsoon (Fig. 21c), where most models see correlation off the northwestern coast of the continent. For the other monsoons considered here, there is no consistent relationship with OH, with MERRA2 GMI being the only model showing correlations with most monsoons (Fig. S16). While models and observations have shown the monsoons can change OH abundance, particularly in the UFT (Lelieveld et al., 2018), the lack of correlation among the models suggests either that those changes are not highly variable from year to year or that not all models capture the mechanisms behind monsoon influence on OH, such as convective lofting of OH precursors.

7.0 Conclusions

Because of limited *in situ* observations and inter-model differences, there is significant uncertainty in the processes driving interannual OH variability, despite its importance in controlling the removal of many atmospheric trace gases. Here, we have explored the relationship between OH and multiple modes of climate variability, including ENSO, the IOD, NH modes of variability, and monsoons in order to understand how these large-scale dynamical features influence OH through control of its dynamical and photochemical drivers.

1235

1236 Using output from the MERRA2 GMI simulation, we have shown that during DJF, when considered
1237 together, these climate features can explain a portion of OH variability over approximately 40% of
1238 the troposphere by mass. ENSO is the dominant mode of variability in all seasons except for JJA and
1239 can explain 20 – 30 % of the spatial variance in TCOH and results in an average decrease in global,
1240 mass weighted OH of 2.2% during El Niño events. Effects from the other modes of variability
1241 considered here are more limited in spatial scale but can strongly alter the atmospheric oxidative
1242 capacity on the local scale. For example, changes in TCOH for the NAO, IOD, and Australian
1243 monsoon can reach 0.5, 1.5, and 7 x 10^{11} molecules/cm^2, respectively, compared to 2 x 10^{11}
1244 molecules/cm^2 for ENSO.

1245

1246 Changes in OH with ENSO are driven by different processes in the upper and lower troposphere. In
1247 the PBL, where OH production is dominated by the reaction of O^1D with water, changes in the
1248 distribution of these species leads to a positive correlation between OH and ENSO. Increases in
1249 $H_2O_{(v)}$ during El Niño are associated with increased convection and warmer SSTs, while increases in
1250 O^1D result from increased horizontal advection of O_3 in the western Pacific and increased
1251 photolysis rates resulting from reduced stratospheric O_3 in the eastern Pacific. In the upper
1252 troposphere, NO controls the OH abundance over the tropical Pacific. In much of the region,
1253 decreases in lightning NO production correspond to decreases in total NO, and thus OH. In the
1254 equatorial region, however, increases in lightning NO production are offset by other processes,
1255 potentially including transport due to changes in the Walker Circulation. Further work is needed to
1256 determine the relative importance of these two factors in controlling OH in the region during El
1257 Niño and La Niña events.

1258

1259 Absolute changes in OH concentration during El Niño and La Niña events in the LFT and, to a lesser
1260 extent, the MFT, were limited by competing effects from changes in the O^1D + H_2O and NO + HO_2
1261 reactions. As a result, ENSO only explains 11.7% of the variability in the LFT and is associated with
1262 the second EOF. Because OH variability in the LFT drives variability in the CH_4 lifetime, which
1263 showed limited response to ENSO variability, further research is warranted to understand the
1264 dominant mode of OH variability at this level, including any impacts in emissions trends, which
1265 appear to be the dominant mode of variability in the PBL.

1266

1267 The relationship between the individual climate modes seen in MERRA2 GMI is also seen in the
1268 majority of the CCMI models, suggesting that the relationship between the modes and OH is robust.
1269 4 of the 5 models examined here show similar relationships between ENSO and TCOH for all
1270 seasons except MAM, and three of those models suggest that ENSO is the dominant mode of OH
1271 variability in DJF, responsible for between 30 and 50% of total spatial variance. Similar agreement
1272 is found for the NH modes of variability and the IOD, while there is little agreement among models
1273 between the relationship of the individual monsoons and OH.

1274

1275 Despite the agreement among models in the importance of the driving factors of OH variability,
1276 there is still a lack of observations to demonstrate that the models are accurate. We have shown
1277 here that satellite observations of H_2O, CO, lightning flashes, and, to a lesser extent, NO_2 are able to
1278 capture the respective variability of each variable as well as the relationship with ENSO, in excellent
1279 agreement with the model simulation. While further understanding of the relationship between
1280 these species and ENSO is needed, the results presented here suggest that combining the
1281 observations of OH drivers and the various climate modes could lead to additional methods to
1282 constrain OH from space.

1283

1284 **Data Availability**

1297 All output from MERRA2 GMI is publicly available at https://acd-
1298 ext.gsfc.nasa.gov/Projects/GEOSCCM/MERRA2GMI/. Output from the EMAC, MRI, and CHASER
1299 models is available from the Centre for Environmental Data Analysis at
1300 http://data.ceda.ac.uk/badc/wcrp-ccmi/data/CCMI-1/output. Output from WACCM are available
1301 at http://www.earthsystemgrid.org. Satellite data are available at https://disc.gsfc.nasa.gov. Data
1302 from the ATom campaign are located at https://espoarchive.nasa.gov/archive/browse/atom.
1303

1304 **Author Contributions**
1305 DCA performed the analysis and wrote the manuscript. All authors contributed ideas for the
1306 analysis and helped revise and improve the manuscript.

1307

1308 **Competing Interests**
1309 The authors declare no competing interests.

1310

1311 **Acknowledgements**
1312 The authors acknowledge funding from the NASA ACMAP program (16-ACMAP16-0027). We
1313 acknowledge the modeling groups for making their simulations available for this analysis, the joint
1314 WCRP SPARC/IGAC Chemistry-Climate Model Initiative (CCMI) for organizing and coordinating the
1315 model data analysis activity, and the British Atmospheric Data Centre (BADC) for collecting and
1316 archiving the CCMI model output.

1317
1318

1319
1320 **References**
1321
1322 Allen, D., Pickering, K., Duncan, B., and Damon, M.: Impact of lightning NO emissions on North
1323 American photochemistry as determined using the Global Modeling Initiative (GMI) model, Journal
1324 of Geophysical Research, 115, 10.1029/2010jd014062, 2010.

1325 Anderson, D. C., Nicely, J. M., Wolfe, G. M., Hanisco, T. F., Salawitch, R. J., Canty, T. P., Dickerson, R. R.,
1326 Apel, E. C., Baidar, S., Bannan, T. J., Blake, N. J., Chen, D. X., Dix, B., Fernandez, R. P., Hall, S. R.,
1327 Hornbrook, R. S., Huey, L. G., Josse, B., Jockel, P., Kinnison, D. E., Koenig, T. K., Le Breton, M., Marecal,
1328 V., Morgenstern, O., Oman, L. D., Pan, L. L., Percival, C., Plummer, D., Revell, L. E., Rozanov, E., Saiz-
1329 Lopez, A., Stenke, A., Sudo, K., Tilmes, S., Ullmann, K., Volkamer, R., Weinheimer, A. J., and Zeng, G.:
1330 Formaldehyde in the Tropical Western Pacific: Chemical Sources and Sinks, Convective Transport,
1331 and Representation in CAM-Chem and the CCMI Models, Journal of Geophysical Research-
1332 Atmospheres, 122, 11201-11226, 10.1002/2016jd026121, 2017.

1333 Barnston, A. G., and Livezey, R. E.: Classification, Seasonality and Persistence of Low-Frequency
1334 Atmospheric Circulation Patterns, Monthly Weather Review, 115, 1083-1126, 10.1175/1520-
1335 0493(1987)115<1083:CSAPOL>2.0.CO;2, 1987.

1336 Borlace, S., Santoso, A., Cai, W., and Collins, M.: Extreme swings of the South Pacific Convergence
1337 Zone and the different types of El Niño events, Geophysical Research Letters, 41, 4695-4703,
1338 10.1002/2014gl060551, 2014.

1339 Bosilovich, M. G., Akella, S., Coy, L., Cullather, R., Draper, C., Gelaro, R., Kovach, R., Liu, Q., Molod, A.,
1340 Norris, P., Wargan, K., Chao, W., Reichle, R., Takacs, L., Vikhliaev, Y., Bloom, S., Collow, A., Firth, S.,
1341 Labow, G., Partyka, G., Pawson, S., Reale, O., Schubert, S. D., and Suarez, M.: MERRA-2: Initial
1342 Evaluation of the Climate, Technical Report Series on Global Modeling and Data Assimilation, 43,
1343 2015.

1344 Brune, W. H., Miller, D. O., Thames, A. B., Allen, H. M., Apel, E. C., Blake, D. R., Bui, T. P., Commane, R.,
1345 Crounse, J. D., Daube, B. C., Diskin, G. S., DiGangi, J. P., Elkins, J. W., Hall, S. R., Hanisco, T. F., Hannun,
1346 R. A., Hintsa, E. J., Hornbrook, R. S., Kim, M. J., McKain, K., Moore, F. L., Neuman, J. A., Nicely, J. M.,
1347 Peischl, J., Ryerson, T. B., St. Clair, J. M., Sweeney, C., Teng, A. P., Thompson, C., Ullmann, K., Veres, P.
1348 R., Wennberg, P. O., and Wolfe, G. M.: Exploring Oxidation in the Remote Free Troposphere: Insights
1349 From Atmospheric Tomography (ATom), Journal of Geophysical Research: Atmospheres, 125,
1350 10.1029/2019jd031685, 2020.

1351 Buchholz, R. R., Hammerling, D., Worden, H. M., Deeter, M. N., Emmons, L. K., Edwards, D. P., and
1352 Monks, S. A.: Links Between Carbon Monoxide and Climate Indices for the Southern Hemisphere
1353 and Tropical Fire Regions, Journal of Geophysical Research: Atmospheres, 123, 9786-9800,
1354 10.1029/2018jd028438, 2018.

1355 Cecil, D. J., Buechler, D. E., and Blakeslee, R. J.: Gridded lightning climatology from TRMM-LIS and
1356 OTD: Dataset description, Atmospheric Research, 135, 404-414, 10.1016/j.atmosres.2012.06.028,
1357 2014.

1358 Creilson, J. K., Fishman, J., and Wozniak, A. E.: Intercontinental transport of tropospheric ozone: a
1359 study of its seasonal variability across the North Atlantic utilizing tropospheric ozone residuals and

Formatted: Font: Cambria

its relationship to the North Atlantic Oscillation, Atmos. Chem. Phys., 3, 2053-2066, 10.5194/acp-3-2053-2003, 2003.

Deeter, M. N., Edwards, D. P., Francis, G. L., Gille, J. C., Mao, D., Martínez-Alonso, S., Worden, H. M., Ziskin, D., and Andreae, M. O.: Radiance-based retrieval bias mitigation for the MOPITT instrument: the version 8 product, Atmospheric Measurement Techniques, 12, 4561-4580, 10.5194/amt-12-4561-2019, 2019.

Dhomse, S. S., Kinnison, D., Chipperfield, M. P., Salawitch, R. J., Cionni, I., Hegglin, M. I., Abraham, N. L., Akiyoshi, H., Archibald, A. T., Bednarz, E. M., Bekki, S., Braesicke, P., Butchart, N., Dameris, M., Deushi, M., Frith, S., Hardiman, S. C., Hassler, B., Horowitz, L. W., Hu, R.-M., Jöckel, P., Josse, B., Kirner, O., Kremser, S., Langematz, U., Lewis, J., Marchand, M., Lin, M., Mancini, E., Marécal, V., Michou, M., Morgenstern, O., amp, apos, Connor, F. M., Oman, L., Pitari, G., Plummer, D. A., Pyle, J. A., Revell, L. E., Rozanov, E., Schofield, R., Stenke, A., Stone, K., Sudo, K., Tilmes, S., Visioni, D., Yamashita, Y., and Zeng, G.: Estimates of ozone return dates from Chemistry-Climate Model Initiative simulations, Atmospheric Chemistry and Physics, 18, 8409-8438, 10.5194/acp-18-8409-2018, 2018.

Dlugokencky, E. J., Steele, L. P., Lang, P. M., and Masarie, K. A.: The growth rate and distribution of atmospheric methane, Journal of Geophysical Research: Atmospheres, 99, 17021-17043, https://doi.org/10.1029/94JD01245, 1994.

Duncan, B. N.: Indonesian wildfires of 1997: Impact on tropospheric chemistry, Journal of Geophysical Research, 108, 10.1029/2002jd003195, 2003a.

Duncan, B. N.: Interannual and seasonal variability of biomass burning emissions constrained by satellite observations, Journal of Geophysical Research, 108, 10.1029/2002jd002378, 2003b.

Duncan, B. N.: A modeling study of the export pathways of pollution from Europe: Seasonal and interannual variations (1987–1997), Journal of Geophysical Research, 109, 10.1029/2003jd004079, 2004.

Duncan, B. N., Logan, J. A., Bey, I., Megretskaia, I. A., Yantosca, R. M., Novelli, P. C., Jones, N. B., and Rinsland, C. P.: Global budget of CO, 1988–1997: Source estimates and validation with a global model, Journal of Geophysical Research, 112, 10.1029/2007jd008459, 2007.

Fisher, J. A., Jacob, D. J., Purdy, M. T., Kopacz, M., Le Sager, P., Carouge, C., Holmes, C. D., Yantosca, R. M., Batchelor, R. L., Strong, K., Diskin, G. S., Fuelberg, H. E., Holloway, J. S., Hyer, E. J., McMillan, W. W., Warner, J., Streets, D. G., Zhang, Q., Wang, Y., and Wu, S.: Source attribution and interannual variability of Arctic pollution in spring constrained by aircraft (ARCTAS, ARCPAC) and satellite (AIRS) observations of carbon monoxide, Atmos. Chem. Phys., 10, 977-996, 10.5194/acp-10-977-2010, 2010.

Gelaro, R., McCarty, W., Suarez, M. J., Todling, R., Molod, A., Takacs, L., Randles, C., Darmenov, A., Bosilovich, M. G., Reichle, R., Wargan, K., Coy, L., Cullather, R., Draper, C., Akella, S., Buchard, V., Conaty, A., da Silva, A., Gu, W., Kim, G. K., Koster, R., Lucchesi, R., Merkova, D., Nielsen, J. E., Partyka, G., Pawson, S., Putman, W., Rienecker, M., Schubert, S. D., Sienkiewicz, M., and Zhao, B.: The Modern-Era Retrospective Analysis for Research and Applications, Version 2 (MERRA-2), J Clim, Volume 30, 5419-5454, 10.1175/JCLI-D-16-0758.1, 2017.

1399 Giglio, L., Randerson, J. T., and van der Werf, G. R.: Analysis of daily, monthly, and annual burned
1400 area using the fourth-generation global fire emissions database (GFED4), Journal of Geophysical
1401 Research: Biogeosciences, 118, 317-328, 10.1002/jgrg.20042, 2013.

1402 Granier, C., Bessagnet, B., Bond, T., D'Angiola, A., Denier van der Gon, H., Frost, G. J., Heil, A., Kaiser, J.
1403 W., Kinne, S., Klimont, Z., Kloster, S., Lamarque, J.-F., Liousse, C., Masui, T., Meleux, F., Mieville, A.,
1404 Ohara, T., Raut, J.-C., Riahi, K., Schultz, M. G., Smith, S. J., Thompson, A., van Aardenne, J., van der
1405 Werf, G. R., and van Vuuren, D. P.: Evolution of anthropogenic and biomass burning emissions of air
1406 pollutants at global and regional scales during the 1980–2010 period, Climatic Change, 109, 163-
1407 190, 10.1007/s10584-011-0154-1, 2011.

1408 Guenther, A., Baugh, B., Brasseur, G., Greenberg, J., Harley, P., Klinger, L., Serça, D., and Vierling, L.:
1409 Isoprene emission estimates and uncertainties for the central African EXPRESSO study domain,
1410 Journal of Geophysical Research: Atmospheres, 104, 30625-30639, 10.1029/1999JD900391, 1999.

1411 Guenther, A., Geron, C., Pierce, T., Lamb, B., Harley, P., and Fall, R.: Natural emissions of non-
1412 methane volatile organic compounds, carbon monoxide, and oxides of nitrogen from North
1413 America, Atmospheric Environment, 34, 2205-2230, https://doi.org/10.1016/S1352-
1414 2310(99)00465-3, 2000.

1415 Jöckel, P., Tost, H., Pozzer, A., Kunze, M., Kirner, O., Brenninkmeijer, C. A. M., Brinkop, S., Cai, D. S.,
1416 Dyroff, C., Eckstein, J., Frank, F., Garny, H., Gottschaldt, K. D., Graf, P., Grewe, V., Kerkweg, A., Kern, B.,
1417 Matthes, S., Mertens, M., Meul, S., Neumaier, M., Nützel, M., Oberländer-Hayn, S., Ruhnke, R., Runde,
1418 T., Sander, R., Scharffe, D., and Zahn, A.: Earth System Chemistry integrated Modelling (ESCiMo)
1419 with the Modular Earth Submodel System (MESSy) version 2.51, Geosci. Model Dev., 9, 1153-1200,
1420 10.5194/gmd-9-1153-2016, 2016.

1421 Lamarque, J. F., Bond, T. C., Eyring, V., Granier, C., Heil, A., Klimont, Z., Lee, D., Liousse, C., Mieville, A.,
1422 Owen, B., Schultz, M. G., Shindell, D., Smith, S. J., Stehfest, E., Van Aardenne, J., Cooper, O. R., Kainuma,
1423 M., Mahowald, N., McConnell, J. R., Naik, V., Riahi, K., and van Vuuren, D. P.: Historical (1850–2000)
1424 gridded anthropogenic and biomass burning emissions of reactive gases and aerosols: methodology
1425 and application, Atmospheric Chemistry and Physics, 10, 7017-7039, 10.5194/acp-10-7017-2010,
1426 2010.

1427 Lamsal, L. N., Krotkov, N. A., Vasilkov, A., Marchenko, S., Qin, W., Yang, E. S., Fasnacht, Z., Joiner, J.,
1428 Choi, S., Haffner, D., Swartz, W. H., Fisher, B., and Bucsela, E.: Ozone Monitoring Instrument (OMI)
1429 Aura nitrogen dioxide standard product version 4.0 with improved surface and cloud treatments,
1430 Atmos. Meas. Tech., 14, 455-479, 10.5194/amt-14-455-2021, 2021.

1431 Lawrence, M. G., Jöckel, P., and von Kuhlmann, R.: What does the global mean OH concentration tell
1432 us?, Atmos. Chem. Phys., 1, 37-49, 10.5194/acp-1-37-2001, 2001.

1433 Lelieveld, J., Bourtsoukidis, E., Bruhl, C., Fischer, H., Fuchs, H., Harder, H., Hofzumahaus, A., Holland,
1434 F., Marno, D., Neumaier, M., Pozzer, A., Schlager, H., Williams, J., Zahn, A., and Ziereis, H.: The South
1435 Asian monsoon-pollution pump and purifier, Science, 361, 270-273, 10.1126/science.aar2501,
1436 2018.

1437 Li, Q., Jacob, D. J., Bey, I., Palmer, P. I., Duncan, B. N., Field, B. D., Martin, R. V., Fiore, A. M., Yantosca, R.
1438 M., Parrish, D. D., Simmonds, P. G., and Oltmans, S. J.: Transatlantic transport of pollution and its

effects on surface ozone in Europe and North America, Journal of Geophysical Research: Atmospheres, 107, ACH 4-1-ACH 4-21, 10.1029/2001JD001422, 2002.

Mao, J., Ren, X., Brune, W. H., Olson, J. R., Crawford, J. H., Fried, A., Huey, L. G., Cohen, R. C., Heikes, B., Singh, H. B., Blake, D. R., Sachse, G. W., Diskin, G. S., Hall, S. R., and Shetter, R. E.: Airborne measurement of OH reactivity during INTEX-B, Atmos. Chem. Phys., 9, 163-173, 10.5194/acp-9-163-2009, 2009.

Melton, J. R., Wania, R., Hodson, E. L., Poulter, B., Ringeval, B., Spahni, R., Bohn, T., Avis, C. A., Beerling, D. J., Chen, G., Eliseev, A. V., Denisov, S. N., Hopcroft, P. O., Lettenmaier, D. P., Riley, W. J., Singarayer, J. S., Subin, Z. M., Tian, H., Zürcher, S., Brovkin, V., van Bodegom, P. M., Kleinen, T., Yu, Z. C., and Kaplan, J. O.: Present state of global wetland extent and wetland methane modelling: conclusions from a model inter-comparison project (WETCHIMP), Biogeosciences, 10, 753-788, 10.5194/bg-10-753-2013, 2013.

Morgenstern, O., Hegglin, M. I., Rozanov, E., amp, apos, Connor, F. M., Abraham, N. L., Akiyoshi, H., Archibald, A. T., Bekki, S., Butchart, N., Chipperfield, M. P., Deushi, M., Dhomse, S. S., Garcia, R. R., Hardiman, S. C., Horowitz, L. W., Jöckel, P., Josse, B., Kinnison, D., Lin, M., Mancini, E., Manyin, M. E., Marchand, M., Marécal, V., Michou, M., Oman, L. D., Pitari, G., Plummer, D. A., Revell, L. E., Saint-Martin, D., Schofield, R., Stenke, A., Stone, K., Sudo, K., Tanaka, T. Y., Tilmes, S., Yamashita, Y., Yoshida, K., and Zeng, G.: Review of the global models used within phase 1 of the Chemistry–Climate Model Initiative (CCMI), Geoscientific Model Development, 10, 639-671, 10.5194/gmd-10-639-2017, 2017.

Murray, L. T., Logan, J. A., and Jacob, D. J.: Interannual variability in tropical tropospheric ozone and OH: The role of lightning, Journal of Geophysical Research: Atmospheres, 118, 11,468-411,480, 10.1002/jgrd.50857, 2013.

Murray, L. T., Mickley, L. J., Kaplan, J. O., Sofen, E. D., Pfeiffer, M., and Alexander, B.: Factors controlling variability in the oxidative capacity of the troposphere since the Last Glacial Maximum, Atmospheric Chemistry and Physics, 14, 3589-3622, 10.5194/acp-14-3589-2014, 2014.

Myers, D. S., and Waliser, D. E.: Three-Dimensional Water Vapor and Cloud Variations Associated with the Madden–Julian Oscillation during Northern Hemisphere Winter, Journal of Climate, 16, 929-950, 10.1175/1520-0442(2003)016<0929:TDWVAC>2.0.CO;2, 2003.

Naik, V., Voulgarakis, A., Fiore, A. M., Horowitz, L. W., Lamarque, J. F., Lin, M., Prather, M. J., Young, P. J., Bergmann, D., Cameron-Smith, P. J., Cionni, I., Collins, W. J., Dalsøren, S. B., Doherty, R., Eyring, V., Faluvegi, G., Folberth, G. A., Josse, B., Lee, Y. H., MacKenzie, I. A., Nagashima, T., van Noije, T. P. C., Plummer, D. A., Righi, M., Rumbold, S. T., Skeie, R., Shindell, D. T., Stevenson, D. S., Strode, S., Sudo, K., Szopa, S., and Zeng, G.: Preindustrial to present-day changes in tropospheric hydroxyl radical and methane lifetime from the Atmospheric Chemistry and Climate Model Intercomparison Project (ACCMIP), Atmospheric Chemistry and Physics, 13, 5277-5298, 10.5194/acp-13-5277-2013, 2013.

Nicely, J. M., Salawitch, R. J., Canty, T., Anderson, D. C., Arnold, S. R., Chipperfield, M. P., Emmons, L. K., Flemming, J., Huijnen, V., Kinnison, D. E., Lamarque, J.-F., Mao, J., Monks, S. A., Steenrod, S. D., Tilmes, S., and Turquety, S.: Quantifying the causes of differences in tropospheric OH within global models, Journal of Geophysical Research: Atmospheres, n/a-n/a, 10.1002/2016JD026239, 2017.

Nicely, J. M., Duncan, B. N., Hanisco, T. F., Wolfe, G. M., Salawitch, R. J., Deushi, M., Haslerud, A. S., Jöckel, P., Josse, B., Kinnison, D. E., Klekociuk, A., Manyin, M. E., Marécal, V., Morgenstern, O., Murray, L. T., Myhre, G., Oman, L. D., Pitari, G., Pozzer, A., Quaglia, I., Revell, L. E., Rozanov, E., Stenke, A., Stone, K., Strahan, S., Tilmes, S., Tost, H., Westervelt, D. M., and Zeng, G.: A machine learning examination of hydroxyl radical differences among model simulations for CCMI-1, Atmospheric Chemistry and Physics, 20, 1341-1361, 10.5194/acp-20-1341-2020, 2020.

Nisbet, E. G., Dlugokencky, E. J., Manning, M. R., Lowry, D., Fisher, R. E., France, J. L., Michel, S. E., Miller, J. B., White, J. W. C., Vaughn, B., Bousquet, P., Pyle, J. A., Warwick, N. J., Cain, M., Brownlow, R., Zazzeri, G., Lanoisellé, M., Manning, A. C., Gloor, E., Worthy, D. E. J., Brunke, E. G., Labuschagne, C., Wolff, E. W., and Ganesan, A. L.: Rising atmospheric methane: 2007-2014 growth and isotopic shift, Global Biogeochemical Cycles, 30, 1356-1370, 10.1002/2016gb005406, 2016.

Oman, L. D., Ziemke, J. R., Douglass, A. R., Waugh, D. W., Lang, C., Rodriguez, J. M., and Nielsen, J. E.: The response of tropical tropospheric ozone to ENSO, Geophysical Research Letters, 38, n/a-n/a, 10.1029/2011gl047865, 2011.

Oman, L. D., Douglass, A. R., Ziemke, J. R., Rodriguez, J. M., Waugh, D. W., and Nielsen, J. E.: The ozone response to ENSO in Aura satellite measurements and a chemistry-climate simulation, Journal of Geophysical Research-Atmospheres, 118, 965-976, 10.1029/2012jd018546, 2013.

Orbe, C., Oman, L. D., Strahan, S. E., Waugh, D. W., Pawson, S., Takacs, L. L., and Molod, A. M.: Large-Scale Atmospheric Transport in GEOS Replay Simulations, Journal of Advances in Modeling Earth Systems, 9, 2545-2560, 10.1002/2017ms001053, 2017.

Orbe, C., Plummer, D. A., Waugh, D. W., Yang, H., Jöckel, P., Kinnison, D. E., Josse, B., Marecal, V., Deushi, M., Abraham, N. L., Archibald, A. T., Chipperfield, M. P., Dhomse, S., Feng, W., and Bekki, S.: Description and Evaluation of the specified-dynamics experiment in the Chemistry-Climate Model Initiative, Atmospheric Chemistry and Physics, 20, 3809-3840, 10.5194/acp-20-3809-2020, 2020.

Pan, L. L., Randel, W. J., Gary, B. L., Mahoney, M. J., and Hintsa, E. J.: Definitions and sharpness of the extratropical tropopause: A trace gas perspective, Journal of Geophysical Research: Atmospheres, 109, n/a-n/a, 10.1029/2004JD004982, 2004.

Prather, M. J., and Holmes, C. D.: Overexplaining or underexplaining methane's role in climate change, Proc Natl Acad Sci U S A, 114, 5324-5326, 10.1073/pnas.1704884114, 2017.

Prinn, R. G., Huang, J., Weiss, R. F., Cunnold, D. M., Fraser, P. J., Simmonds, P. G., McCulloch, A., Harth, C., Salameh, P., O'Do, Wang, R. H. J., Porter, L., and Miller, B. R.: Evidence for Substantial Variations of Atmospheric Hydroxyl Radicals in the Past Two Decades, Science, 292, 1882-1888, 10.1126/science.1058673, 2001.

Randel, W. J., Garcia, R. R., Calvo, N., and Marsh, D.: ENSO influence on zonal mean temperature and ozone in the tropical lower stratosphere, Geophysical Research Letters, 36, 10.1029/2009GL039343, 2009.

Revell, L. E., Stenke, A., Tummon, F., Feinberg, A., Rozanov, E., Peter, T., Abraham, N. L., Akiyoshi, H., Archibald, A. T., Butchart, N., Deushi, M., Jöckel, P., Kinnison, D., Michou, M., Morgenstern, O., amp, apos, Connor, F. M., Oman, L. D., Pitari, G., Plummer, D. A., Schofield, R., Stone, K., Tilmes, S., Visioni, D., Yamashita, Y., and Zeng, G.: Tropospheric ozone in CCMI models and Gaussian process emulation

to understand biases in the SOCOLv3 chemistry–climate model, Atmospheric Chemistry and Physics, 18, 16155-16172, 10.5194/acp-18-16155-2018, 2018.

Rigby, M., Montzka, S. A., Prinn, R. G., White, J. W. C., Young, D., O'Doherty, S., Lunt, M. F., Ganesan, A. L., Manning, A. J., Simmonds, P. G., Salameh, P. K., Harth, C. M., Muhle, J., Weiss, R. F., Fraser, P. J., Steele, L. P., Krummel, P. B., McCulloch, A., and Park, S.: Role of atmospheric oxidation in recent methane growth, Proc Natl Acad Sci U S A, 114, 5373-5377, 10.1073/pnas.1616426114, 2017.

Rowlinson, M. J., Rap, A., Arnold, S. R., Pope, R. J., Chipperfield, M. P., McNorton, J., Forster, P., Gordon, H., Pringle, K. J., Feng, W., Kerridge, B. J., Latter, B. L., and Siddans, R.: Impact of El Niño–Southern Oscillation on the interannual variability of methane and tropospheric ozone, Atmospheric Chemistry and Physics, 19, 8669-8686, 10.5194/acp-19-8669-2019, 2019.

Santoni, G. W., Daube, B. C., Kort, E. A., Jiménez, R., Park, S., Pittman, J. V., Gottlieb, E., Xiang, B., Zahniser, M. S., Nelson, D. D., McManus, J. B., Peischl, J., Ryerson, T. B., Holloway, J. S., Andrews, A. E., Sweeney, C., Hall, B., Hintsa, E. J., Moore, F. L., Elkins, J. W., Hurst, D. F., Stephens, B. B., Bent, J., and Wofsy, S. C.: Evaluation of the airborne quantum cascade laser spectrometer (QCLS) measurements of the carbon and greenhouse gas suite - CO2, CH4, N2O, and CO - during the CalNex and HIPPO campaigns, Atmospheric Measurement Techniques, 7, 1509-1526, 10.5194/amt-7-1509-2014, 2014.

Seibert, P., Beyrich, F., Gryning, S.-E., Joffre, S., Rasmussen, A., and Tercier, P.: Review and intercomparison of operational methods for determination of the mixing height, Atmospheric Environment, 34, 1001-1027, 2000.

Sekiya, T., and Sudo, K.: Role of meteorological variability in global tropospheric ozone during 1970-2008, Journal of Geophysical Research: Atmospheres, 117, n/a-n/a, 10.1029/2012jd018054, 2012.

Shi, L., Schreck, C., and Schröder, M.: Assessing the Pattern Differences between Satellite-Observed Upper Tropospheric Humidity and Total Column Water Vapor during Major El Niño Events, Remote Sensing, 10, 10.3390/rs10081188, 2018.

Solomon, S., Kinnison, D., Bandoro, J., and Garcia, R.: Simulation of polar ozone depletion: An update, Journal of Geophysical Research: Atmospheres, 120, 7958-7974, 10.1002/2015jd023365, 2015.

Spivakovsky, C. M., Logan, J. A., Montzka, S. A., Balkanski, Y. J., Foreman-Fowler, M., Jones, D. B. A., Horowitz, L. W., Fusco, A. C., Brenninkmeijer, C. A. M., Prather, M. J., Wofsy, S. C., and McElroy, M. B.: Three-dimensional climatological distribution of tropospheric OH: Update and evaluation, Journal of Geophysical Research: Atmospheres, 105, 8931-8980, 10.1029/1999jd901006, 2000.

Stein, O., Schultz, M. G., Bouarar, I., Clark, H., Huijnen, V., Gaudel, A., George, M., and Clerbaux, C.: On the wintertime low bias of Northern Hemisphere carbon monoxide found in global model simulations, Atmospheric Chemistry and Physics, 14, 9295-9316, 10.5194/acp-14-9295-2014, 2014.

Stone, D., Whalley, L. K., and Heard, D. E.: Tropospheric OH and HO2 radicals: field measurements and model comparisons, Chem Soc Rev, 41, 6348-6404, 10.1039/c2cs35140d, 2012.

Strode, S. A., Ziemke, J. R., Oman, L. D., Lamsal, L. N., Olsen, M. A., and Liu, J.: Global changes in the diurnal cycle of surface ozone, Atmospheric Environment, 199, 323-333, 10.1016/j.atmosenv.2018.11.028, 2019.

Susskind, J., Blaisdell, J. M., and Iredell, L.: Improved methodology for surface and atmospheric soundings, error estimates, and quality control procedures: the atmospheric infrared sounder science team version-6 retrieval algorithm, Journal of Applied Remote Sensing, 8, 10.1117/1.Jrs.8.084994, 2014.

Tian, B., Yung, Y. L., Waliser, D. E., Tyranowski, T., Kuai, L., Fetzer, E. J., and Irion, F. W.: Intraseasonal variations of the tropical total ozone and their connection to the Madden-Julian Oscillation, Geophysical Research Letters, 34, 10.1029/2007gl029451, 2007.

Travis, K. R., Heald, C. L., Allen, H. M., Apel, E. C., Arnold, S. R., Blake, D. R., Brune, W. H., Chen, X., Commane, R., Crounse, J. D., Daube, B. C., Diskin, G. S., Elkins, J. W., Evans, M. J., Hall, S. R., Hintsa, E. J., Hornbrook, R. S., Kasibhatla, P. S., Kim, M. J., Luo, G., McKain, K., Millet, D. B., Moore, F. L., Peischl, J., Ryerson, T. B., Sherwen, T., Thames, A. B., Ullmann, K., Wang, X., Wennberg, P. O., Wolfe, G. M., and Yu, F.: Constraining remote oxidation capacity with ATom observations, Atmospheric Chemistry and Physics, 20, 7753-7781, 10.5194/acp-20-7753-2020, 2020.

Turner, A. J., Frankenberg, C., Wennberg, P. O., and Jacob, D. J.: Ambiguity in the causes for decadal trends in atmospheric methane and hydroxyl, Proceedings of the National Academy of Sciences, 114, 5367, 10.1073/pnas.1616020114, 2017.

Turner, A. J., Fung, I., Naik, V., Horowitz, L. W., and Cohen, R. C.: Modulation of hydroxyl variability by ENSO in the absence of external forcing, Proc Natl Acad Sci U S A, 115, 8931-8936, 10.1073/pnas.1807532115, 2018.

Voulgarakis, A., Naik, V., Lamarque, J. F., Shindell, D. T., Young, P. J., Prather, M. J., Wild, O., Field, R. D., Bergmann, D., Cameron-Smith, P., Cionni, I., Collins, W. J., Dalsøren, S. B., Doherty, R. M., Eyring, V., Faluvegi, G., Folberth, G. A., Horowitz, L. W., Josse, B., MacKenzie, I. A., Nagashima, T., Plummer, D. A., Righi, M., Rumbold, S. T., Stevenson, D. S., Strode, S. A., Sudo, K., Szopa, S., and Zeng, G.: Analysis of present day and future OH and methane lifetime in the ACCMIP simulations, Atmospheric Chemistry and Physics, 13, 2563-2587, 10.5194/acp-13-2563-2013, 2013.

Wang, P., Schade, G., Estes, M., and Ying, Q.: Improved MEGAN predictions of biogenic isoprene in the contiguous United States, Atmospheric Environment, 148, 337-351, 10.1016/j.atmosenv.2016.11.006, 2017.

Watanabe, S., Hajima, T., Sudo, K., Nagashima, T., Takemura, T., Okajima, H., Nozawa, T., Kawase, H., Abe, M., Yokohata, T., Ise, T., Sato, H., Kato, E., Takata, K., Emori, S., and Kawamiya, M.: MIROC-ESM 2010: model description and basic results of CMIP5-20c3m experiments, Geosci. Model Dev., 4, 845-872, 10.5194/gmd-4-845-2011, 2011.

Wild, O., Voulgarakis, A., amp, apos, Connor, F., Lamarque, J.-F., Ryan, E. M., and Lee, L.: Global sensitivity analysis of chemistry-climate model budgets of tropospheric ozone and OH: exploring model diversity, Atmospheric Chemistry and Physics, 20, 4047-4058, 10.5194/acp-20-4047-2020, 2020.

Wolfe, G. M., Nicely, J. M., St Clair, J. M., Hanisco, T. F., Liao, J., Oman, L. D., Brune, W. B., Miller, D., Thames, A., Gonzalez Abad, G., Ryerson, T. B., Thompson, C. R., Peischl, J., McCain, K., Sweeney, C., Wennberg, P. O., Kim, M., Crounse, J. D., Hall, S. R., Ullmann, K., Diskin, G., Bui, P., Chang, C., and Dean-Day, J.: Mapping hydroxyl variability throughout the global remote troposphere via synthesis of airborne and satellite formaldehyde observations, Proc Natl Acad Sci U S A, 116, 11171-11180, 10.1073/pnas.1821661116, 2019.

Wolter, K., and Timlin, M. S.: El Niño/Southern Oscillation behaviour since 1871 as diagnosed in an extended multivariate ENSO index (MEI.ext), International Journal of Climatology, 31, 1074-1087, 10.1002/joc.2336, 2011.

Wong, S., and Dessler, A. E.: Regulation of H2O and CO in tropical tropopause layer by the Madden-Julian oscillation, Journal of Geophysical Research: Atmospheres, 112, 10.1029/2006JD007940, 2007.

Worden, J., Jiang, Z., Jones, D. B. A., Alvarado, M., Bowman, K., Frankenberg, C., Kort, E. A., Kulawik, S. S., Lee, M., Liu, J., Payne, V., Wecht, K., and Worden, H.: El Niño, the 2006 Indonesian peat fires, and the distribution of atmospheric methane, Geophysical Research Letters, 40, 4938-4943, https://doi.org/10.1002/grl.50937, 2013.

Yim, S.-Y., Wang, B., Liu, J., and Wu, Z.: A comparison of regional monsoon variability using monsoon indices, Climate Dynamics, 43, 1423-1437, 10.1007/s00382-013-1956-9, 2013.

Yukimoto, S., Adachi, Y., Hosaka, M., Sakami, T., Yoshimura, H., Hirabara, M., Tanaka, T. Y., Shindo, E., Tsujino, H., Deushi, M., Mizuta, R., Yabu, S., Obata, A., Nakano, H., Koshiro, T., Ose, T., and Kitoh, A.: A New Global Climate Model of the Meteorological Research Institute: MRI-CGCM3-Model Description and Basic Performance, Journal of the Meteorological Society of Japan. Ser. II, 90A, 23-64, 10.2151/jmsj.2012-A02, 2012.

Zhang, Z., Zimmermann, N. E., Calle, L., Hurtt, G., Chatterjee, A., and Poulter, B.: Enhanced response of global wetland methane emissions to the 2015–2016 El Niño-Southern Oscillation event, Environmental Research Letters, 13, 10.1088/1748-9326/aac939, 2018.

Zhao, Y., Saunois, M., Bousquet, P., Lin, X., Berchet, A., Hegglin, M. I., Canadell, J. G., Jackson, R. B., Hauglustaine, D. A., Szopa, S., Stavert, A. R., Abraham, N. L., Archibald, A. T., Bekki, S., Deushi, M., Jöckel, P., Josse, B., Kinnison, D., Kirner, O., Marécal, V., Connor, F. M., Plummer, D. A., Revell, L. E., Rozanov, E., Stenke, A., Strode, S., Tilmes, S., Dlugokencky, E. J., and Zheng, B.: Inter-model comparison of global hydroxyl radical (OH) distributions and their impact on atmospheric methane over the 2000-2016 period, Atmospheric Chemistry and Physics, 19, 13701-13723, 10.5194/acp-19-13701-2019, 2019.

Ziemke, J. R., Douglass, A. R., Oman, L. D., Strahan, S. E., and Duncan, B. N.: Tropospheric ozone variability in the tropics from ENSO to MJO and shorter timescales, Atmospheric Chemistry and Physics, 15, 8037-8049, 10.5194/acp-15-8037-2015, 2015.

Ziemke, J. R., Oman, L. D., Strode, S. A., Douglass, A. R., Olsen, M. A., McPeters, R. D., Bhartia, P. K., Froidevaux, L., Labow, G. J., Witte, J. C., Thompson, A. M., Haffner, D. P., Kramarova, N. A., Frith, S. M., Huang, L.-K., Jaross, G. R., Seftor, C. J., Deland, M. T., and Taylor, S. L.: Trends in global tropospheric ozone inferred from a composite record of TOMS/OMI/MLS/OMPS satellite measurements and the

1636   MERRA-2 GMI simulation, Atmospheric Chemistry and Physics, 19, 3257-3269, 10.5194/acp-19-
1637   3257-2019, 2019.
1638